University of New Mexico

UNM Digital Repository

Spring 4-26-2022

DC MICROGRID FAULT DETECTION USING MULTIRESOLUTION ANALYSIS OF TRAVELING WAVES

Rudy Montoya
University of New Mexico

Recommended Citation

Rudy Montoya
_____
Candidate

Mechanical Engineering
_____
Department

This thesis is approved, and it is acceptable in quality and form for publication:

Approved by the Thesis Committee:

Dr. Ali Bidram, Chairperson
_____

Dr. Svetlana Prorseva
_____

Dr. Matthew Reno
_____

DC MICROGRID FAULT DETECTION USING
MULTIRESOLUTION ANALYSIS OF TRAVELING WAVES

By

RUDY MONTOYA

Bachelor of Science in Mechanical Engineering

THESIS

Submitted in Partial Fulfillment of the
Requirements for the Degree of

Master of Science in Mechanical Engineering

The University of New Mexico
Albuquerque, New Mexico

May, 2022

DEDICATION

I would like to dedicate this to my wife, Marie, who has inspired me to live up to my full potential. Because of her strength, I was able to complete this journey in my life, and ones that are to come. Thank you.

ACKNOWLEDGEMENTS

I would like to give my unbounded gratitude to my mentor and committee chair, Dr. Ali Bidram, for giving me the opportunity to work under his supervision and for selflessly sharing his knowledge and wisdom. I have learned so much from his teachings and will forever be indebted. I would also like to thank committee member, Dr. Matthew Reno, for his role in furthering my education. I have learned a lot from him and his team at Sandia National Laboratories and now have a high benchmark to strive towards. I will always be grateful for his contributions. Thanks to committee member, Dr. Svetlana Poroseva, for taking her time to be a part of my thesis defense committee. I appreciate all the support she has given and her contributions to the School of Engineering at UNM.

DC MICROGRID FAULT DETECTION USING MULTIRESOLUTION ANALYSIS OF TRAVELING WAVES

By

RUDY MONTOYA

B.S., Mechanical Engineering, University of New Mexico, 2020

M.S., Mechanical Engineering, University of New Mexico, 2022

ABSTRACT

Fast detection and isolation of faults in a DC microgrid is of particular importance. Fast tripping protection (i) increases the lifetime of power electronics (PE) switches by avoiding high fault current magnitudes and (ii) enhances the controllability of PE converters. This thesis proposes a traveling wave (TW) based scheme for fast tripping protection of DC microgrids. The proposed scheme utilizes a discrete wavelet transform (DWT) to calculate the high-frequency components of DC fault currents. Multiresolution analysis (MRA) using DWT is utilized to detect TW components for different frequency ranges. The Parseval energy calculated from the MRA coefficients are then used to demonstrate a quantitative relationship between that energy and the fault current signal energy. The calculated Parseval energy values are used to train a Support Vector Machine classifier to identify the fault type and a Gaussian Process regression engine to estimate the fault location on the DC cables. The proposed approach is verified by simulating two microgrid test systems in PSCAD/EMTDC.

Table of Contents

List of Tables

List of Figures

1. Introduction

1.1 Motivation

Many countries are moving into more technology driven societies from traditionally agrarian ones, and the energy needs of the world will only increase. These developing nations do not have the infrastructure to establish a nationwide electrical grid like the ones prevalent in developed nations [2]. In order to progress into the modern era, access to electricity is vital, and the approach must be on a small scale for many developing nations.

Developed nations also stand to gain from microgrid technology. They can serve the role of a backup system to vital operations that cannot be interrupted without experiencing catastrophic consequences. Examples of these operations are any emergency services, such as hospitals, fire rescue services and police departments. Certain manufacturing or data services could also fall into this category. Some proponents of microgrid systems envision them as being a more key component to grid modernization with them being fully integrated into the larger grid network [3].

Additionally, it is estimated that the supply of fossil fuels will be diminished within this decade [4,5]. Energy has primarily been derived from the burning of fossil fuels, without this source, it is imperative to adopt alternative means of producing energy. The need to innovate and rethink electrical grid infrastructure is important to ensure future generations have an opportunity to thrive.

A solution to this complex problem comes in the form of a microgrid system: a small power plant that can operate autonomously which incorporates as much clean, renewable power sources as possible. The attractiveness of microgrid systems is the

flexibility and modularity of how distributed energy resources (DER's), such as battery storage, fuel cells and PV systems, can be incorporated to meet the specific need of the end users. Whether it is a small, rural community or an individual building, a microgrid can be tailored for the specific purpose.

The electrical grid, in its current form, operates as an AC power system. DC electrical power systems do exist but mainly in the form of electrical transmission. Similarly, there are also AC and DC versions of microgrids, with the former being more well established. DC microgrids do offer an advantage over the AC versions, in the form of efficiency. It is because of these efficiency gains that DC systems are being explored in this thesis.

1.2 Review of DC Systems and Their Protection

DC microgrids render increased efficiency compared to their AC counterparts and flexibility for the integration of DC power sources (e.g., photovoltaic and battery energy storage systems). Due to these advantages, DC microgrids have gained more attention in recent years [6–10]. One of the challenging tasks in DC microgrids' operation is their proper and effective protection. The fault currents in a DC system possess different signatures compared to the AC systems. No zero crossing of current in DC systems makes the interruption of fault currents with fuses and circuit breakers more difficult which, in turn, creates arcing and long fault clearing time [11]. On the other hand, fast detection and isolation of faults in a DC microgrid is of particular importance [12–14]. Due to the presence of power electronics (PE) switches, the DC fault currents usually are associated with a high magnitude that is sustained for a couple of milliseconds and then are attenuated after the internal protection of PE switches operates which blocks the switch operation.

Therefore, the fast detection and isolation of faults are required to: (i) increase the lifetime of PE switches by avoiding high fault current magnitudes, and (ii) enhance the controllability over PE converters under fault scenarios by preventing unwanted PE switches' blocked operation [12–16].

Conventionally, the protection of DC systems is based on overcurrent protection, undervoltage protection, rate of change of current, or differential schemes [17–21]. In [22], cable current derivatives are utilized to detect faults in DC microgrids. Alternatively, traveling wave (TW) protection schemes have been introduced to accommodate a faster tripping protection in electric power grids. These schemes rely on high-frequency measurements. The high-frequency transients can propagate through the system at a speed close to the speed of light. This feature can facilitate fast detection of TWs in less than 1 ms after the fault. Moreover, TW protection does not depend on the magnitude of the fault currents which, in turn, is a good candidate to detect high impedance faults. TW protection is a promising approach for increasing the reliability and resilience of modern power grids with high penetration of renewable energy resources [23–29].

The TW protection of high voltage DC (HVDC) systems is addressed in [30–37]. In [30], the frequency characteristics of TWs are used to develop a protection scheme for HVDC transmission lines. This method uses the first locally measured TW and accounts for the frequency component and polarity of TW rather than its arrival time. In [31], a TW protection technique is proposed that considers the power developed by both the forward and backward TWs. The amount of power transferred by these TWs is used to determine the fault location. In [32], a TW backup protection for a transmission line in an HVDC system is proposed. This reference analyzes the characteristics of TWs for internal and

external fault currents and uses the characteristic differences to develop a backup protection scheme. In [33], a TW protection technique for a converter-based-high-voltage DC transmission line is proposed. This method can detect high resistance pole to ground (PG) faults. In [34], another approach for the protection of line-commutated converter- based-high-voltage DC is proposed that considers the electro-magnetic coupling effect between double circuit HVDC transmission lines. In [35], a TW protection scheme for multiterminal HVDC systems is presented. Continuous wavelet transform is used to calculate the arrival time of the first TWs at all converter stations. In [36], the difference of arrival time between the ground mode and line mode TWs is used for fault detection in multiterminal HVDC systems. In [37], multiterminal differential protection is presented for an HVDC system. This method uses a derivative-based wavelet transform to calculate high-frequency components of fault currents. In [29], a high-speed phaselet-based distance relaying scheme is proposed. Although, there are many TW protection techniques available for HVDC systems, the TW protection of medium voltage DC (MVDC) microgrids is not well studied in the literature. In [14], a TW protection scheme for MVDC microgrids is presented. This scheme requires the first locally measured TW and relies on its waveshape properties and polarity rather than its arrival time. This scheme uses a look-up table to map the waveshape properties and fault scenario. The lookup table should accommodate all possible fault scenarios which can be a challenging task. In [38], wavelet transform and artificial neural networks (ANN) are used to detect and classify faults in an MVDC shipboard power system. The wavelet coefficients' features are used to train ANN for classifying faults. This scheme is only able to detect and classify faults and cannot find their locations on the cables. In [39], a wavelet transform, and ANN are used to detect faults and identify their

type in a DC microgrid. The focus of both [38] and [39] is on fault detection and classification rather than finding the location of the fault along DC microgrid cables. The findings of [40] present a numerical approach to determining fault locations using TWs and MRA. This method utilizes a spline, as well as a power series curve-fitting technique applied to Parseval energy calculated from traveling wave MRA coefficients to determine fault locations. The research of [41] capitalizes on DWT and MRA to calculate Parseval energy and determine fault location and provide fault classification. This research utilizes the methodologies of two state-of-the-art machine learning techniques: Random Forest and Tree Boosting. A comprehensive survey of various traveling wave protection schemes are thoroughly covered in [42].

On the other hand, more recently, machine learning techniques have been proposed as a promising solution for power system protection to further improve its performance. With increased access to real-time and historical data in modern power systems, machine learning algorithms have rendered a great potential for revolutionizing grid protection schemes. Fault detection, location, and response can benefit significantly with the addition of machine learning. A review of machine learning algorithms for power system protection is provided in [43]. Reference [44] uses frequency domain analysis and neural networks for fault location and fault section identification using line currents. In [45], a combined wavelet-transform-extreme learning machine is proposed for fault section identification, classification, and location in a series- compensated transmission line. In [46,47], Support Vector Machine (SVM) is utilized for fault location and classification in transmission systems. In [38,39], and [48], ANN is utilized to detect and classify faults in DC systems. In [49], Gaussian Process (GP) is used to detect faults in a simple DC system.

In this thesis, a TW protection scheme utilizing machine learning (ML) for DC microgrids is proposed. The proposed scheme utilizes discrete wavelet transform (DWT) to calculate the high-frequency components of DC fault currents. Multiresolution analysis (MRA) is used along with DWT to calculate TW components for multiple high frequency ranges. The Parseval energy calculated from the MRA coefficients are then used to demonstrate a quantitative relationship between that energy and the fault current signal energy. The calculated Parseval energies are used to train ML engines to (i) identify the fault type and (ii) estimate the fault location on the DC cables. In this thesis, SVM is used as a classifier for fault type classification. GP is used as the regression tool for estimating fault location. The proposed approach is verified by simulating two microgrid test systems in PSCAD/EMTDC. This thesis makes the following contributions:

- The fast-tripping protection of DC microgrids is addressed by using the TW signatures at different high-frequency ranges.
- The proposed scheme does not require any communication infrastructure and only relies on local measurements for fault detection and location.
- The proposed scheme effectively works for other bolted and resistive pole to pole (PP) and PG faults and can effectively find the fault type, location, and direction.
- DWT and MRA are applied on DC fault current and voltage TWs to not only detect and classify faults but also find the location of the fault along the cables.

The rest of the thesis is organized as follows: Section 2 provides the preliminaries of TWs in a fault condition. In Section 3, the DWT and MRA are introduced. Section 4 elaborates on the characteristics of MRA outputs for faults in a DC system. In Section 5,

our proposed fault detection and location scheme is discussed. Simulation results are provided in Section 6. Section 7 concludes the thesis.

2. Preliminaries on TW Theory

TWs are electromagnetic waves propagated along the power system equipment such as lines or cables when a disturbance (e.g., fault, lightning, switching, etc.) occurs. When the high-frequency TWs reach a new environment with different circuit parameters (e.g., at a line terminal), a portion of the incident TW is reflected while the other portion is refracted to the neighboring equipment. Depending on the circuit parameters at both sides of the terminal, the amplitude of reflected and refracted TWs changes accordingly. The reflected TWs are also reflected and refracted again after they reach the fault location or line terminals [24]. TWs along transmission lines are formulated using the telegrapher's equations. These coupled differential equations relate voltage $v(x,t)$ and current $i(x,t)$ at any point in time and space. In phasor domain, the general solutions to these equations can be described as [23,50]

$$\begin{cases} \tilde{I}(x,t) = I_0^+ e^{-\gamma x} + I_0^- e^{\gamma x}, \\ \tilde{V}(x,t) = V_0^+ e^{-\gamma x} + V_0^- e^{\gamma x}, \end{cases} \tag{1}$$

where I_0^+, I_0^-, V_0^+, and V_0^- are the Laplace transforms of voltage and current TW components (i.e., incident and reflection), x describes the distance from the fault point, and γ denotes the propagation constant. In time domain, one can write the voltage TW equation as

$$\begin{cases} v(x,t) = v^+(x,t) + v^-(x,t), \\ v^+(x,t) = |V_0^+| e^{-\alpha x} \cos(\omega t - \beta x), \\ v^-(x,t) = |V_0^-| e^{\alpha x} \cos(\omega t + \beta x), \end{cases} \tag{2}$$

where α and β denote the attenuation constant and phase constant, respectively. A similar procedure can be used to obtain the equations for $i(x,t)$. The propagation constant is

$$\gamma = \alpha + j\beta. \tag{3}$$

Alternatively, the propagation constant can be formulated as

$$\gamma = \sqrt{(R + j\omega L)(G + j\omega C)}, \tag{4}$$

where R, L, G, and C are the per unit length resistance, inductance, conductance, and capacitance of the transmission line or cable, ω represents the angular frequency of the TW. The propagation velocity of a TW is

$$v = \frac{\omega}{\beta}. \tag{5}$$

In general, higher frequency TWs travel faster but have a larger α and hence a lower magnitude compared to the lower frequency ones.

3. DWT and MRA

The wavelet transform (WT) has been widely utilized as an effective tool for the simultaneous analysis of waveforms in time and frequency domains [51,52]. As opposed to the Fourier Transform where the frequency content is related to the entire duration of the analyzed signal, WT can accommodate localized frequency contents in time. Discrete wavelet transform (DWT) is defined as [38]

$$W_D(m,n) = \frac{1}{\sqrt{a_0^m}} \sum_k x[k] \Psi\left[\frac{k-nb_0 a_0^m}{a_0^m}\right], \tag{6}$$

with Ψ is defined as the mother wavelet, k is discretized time. Variables, m, and n facilitate scaling and time shifting with parameters a_0 and b_0. DWT is subject to the uncertainty principle of signal processing where both time and frequency cannot be located very precisely; the better resolution in frequency would compromise the time resolution and vice versa.

In order to effectively construct wavelets over a wide frequency range, multiresolution analysis (MRA), advanced by Mallat [53], is a practical approach for fully implementing the discrete wavelet transform. MRA details the procedure to obtain an orthonormal wavelet basis with compact support. MRA can be implemented by a series of high-pass and low-pass filters and decimators as shown in Fig. 1. As seen in the figure, the outputs of low and high-pass filters at each level are a_i[n] and d_i[n]. The output of the low-pass filter at each level is passed through the next level for constructing wavelets for the next decomposition level. The low-pass filter outputs are referred to as scaling coefficients while the high-pass filter outputs are called wavelet coefficients. Assuming that the initial sampling frequency of WT is set as f_s, then the frequency range of each level is shown in Fig. 1. In this thesis, the wavelet coefficients are of interest since they better represent the

high-frequency behavior of TWs [38]. According to [54], it is possible to reconstruct the original signal using wavelet series reconstruction. To this end, reverse filters are used to up sample the coefficients by the factor of 2. The reconstruction facilitates the delivery of wavelet coefficients of different scales with a finer resolution.

Once the MRA based wavelet coefficients are identified, the Parseval's theorem is used to calculate the energy corresponding to the identified coefficients. In this thesis, the MRA analysis is conducted on both voltage and current measurements. As discussed in [38,51], if the scaling function and the mother wavelet form an orthonormal basis, then Parseval's theorem can be used to build a relationship between the calculated wavelet coefficients and the energy spectrum of the fault signal (i.e., cable's voltage or current measurement). Under this condition, Parseval's theorem states that the energy of the fault signal can be described mathematically in terms of the expansion coefficients (i.e., the integral or sum of the square of the original function is equal to the sum of the square of the coefficients). The DWT can split the energy of fault signals in time and frequency domains. With Parseval's theorem, one can effectively interpret the high-frequency signatures of TWs by relating the current or voltage TW energy to the energy calculated from the wavelet coefficients. The fault signal can be described by the wavelet coefficients of different ranges. The total Parseval energy of the wavelet coefficients of current or voltage measurements, d_i, at m^{th} time step after an initial time t_0 are defined as [38,51]

$$E_{PRS}(m) = \sum_{i=1}^{n} \sum_{j=1}^{m} d_i^2(t_0 + j\Delta t), \qquad (7)$$

where $d_i(t)$ denotes the wavelet coefficient calculated for the i-th decomposition level at the time t; Δt is the time step used in DWT. The Parseval energy of a single wavelet coefficient that corresponds to a specific MRA level can be described as

$$E_{PRS,i}(m) = \sum_{j=1}^{m} d_i^2(t_0 + j\Delta t). \tag{8}$$

In the following, $E_{PRS,i}(m)$ is calculated for different MRA levels of current and voltage measurements on each cable. $E_{PRS,i}(m)$ values will be analyzed and utilized for the proposed fault detection, classification, and location algorithms.
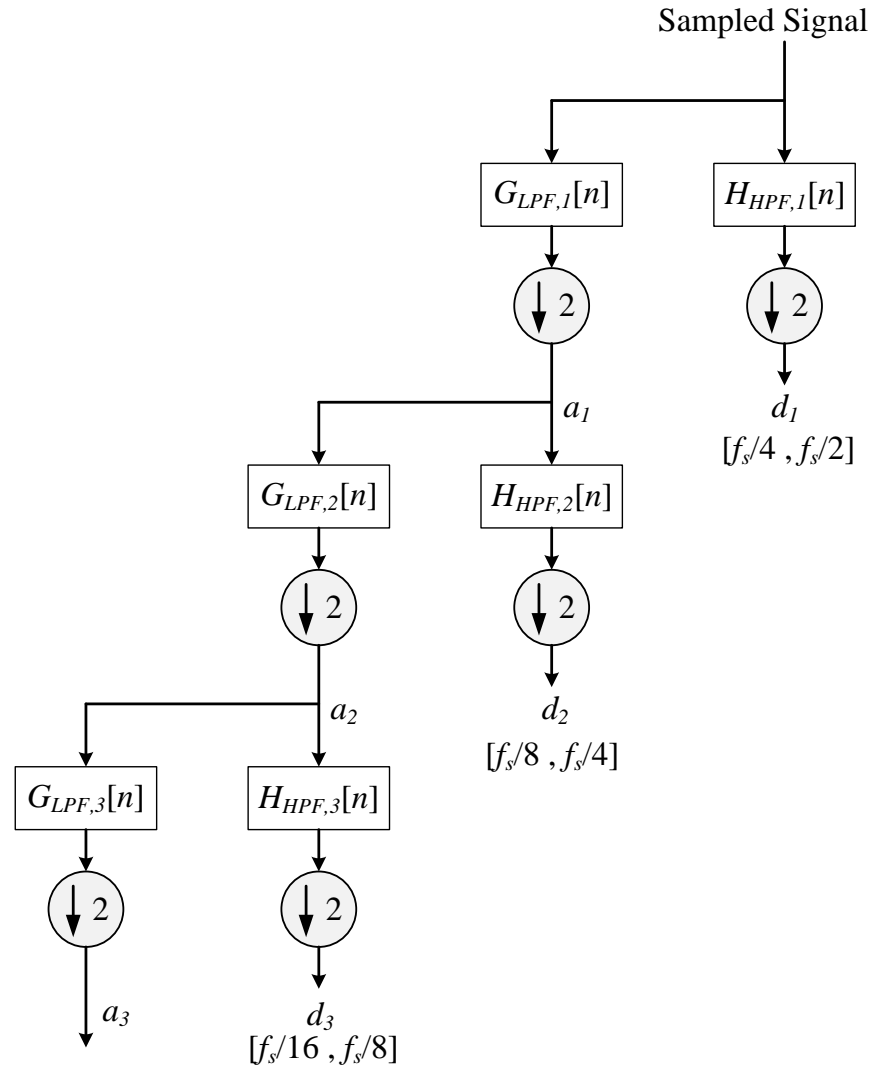
Figure 1. MRA block diagram.

12

4. High-Frequency Fault Signatures in a DC System

4.1. Simple Microgrid Model

In order to study the high-frequency fault signatures of DC systems, a simple DC system (shown in Fig. 2) is modeled in PSCAD/EMTDC. This circuit includes a controllable DC voltage source, one cable with the length of 3000 m, and a DC load with the resistance of 10 Ω. The nominal voltage of this system is $\pm$ 375 V. The cable is modeled using the frequency-dependent distributed parameter model available in PSCAD/EMTDC. The cable specifications are provided in Fig. 3. It is assumed that each pole is buried 1 m deep. The core conductor resistivity is 2×10^{-8} Ωm while sheath resistivity is 30×10^{-8} Ωm.
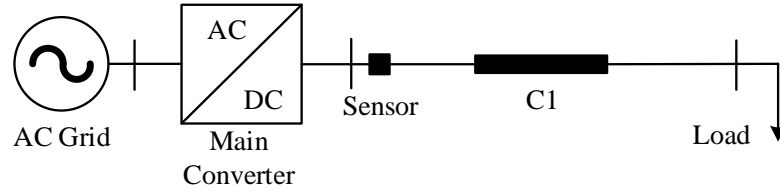
Figure 2. Simple DC microgrid system.
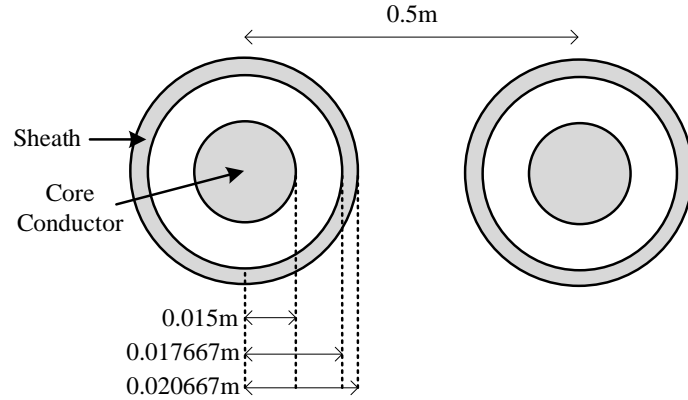
Figure 3. Cable configuration of the DC system in Fig. 2.

4.2. Pole to Pole Fault Characteristics

When a Pole to Pole (PP) fault occurs on a cable, the voltage at the local terminal of cable (i.e. where the sensor is located) hugely drops while the pole current increases significantly and is attained for a short period of time until the internal protection of the main converter PE operates and the pole currents are forced back to zero. To illustrate the high-frequency fault current signatures in a DC system, it is assumed that a PP fault is applied at 2625 m of Cable C1 from the current sensor side. The fault is applied at $t = 0.5$ s. The sensor's current, MRA's level 1 wavelet coefficient, and its Parseval energy are shown in Fig. 4. Fig. 4b clearly illustrates the TW incidents received at the sensor location after the fault occurs. In this study, the sampling frequency of DWT is 1 MHz. Daubechies (db8) is used as the mother wavelet. Therefore, the wavelet coefficient shown in Fig. 4b represents the TW components corresponding to [250 kHz, 500 kHz] frequency range. The Parseval energy, shown in Fig. 4c, demonstrates a quantitative measure of the TWs. As seen, after the first incident of TW arrives at the sensor location, the Parseval energy increases and is settled at an interim value until the next incident TW reaches the sensor location. Using the Parseval energy value, one can identify the timing of TW incidents at different decomposition levels. In this thesis, the Parseval energy of the first incident of TWs is of interest. This value will be later used in the fault classification and location algorithm.
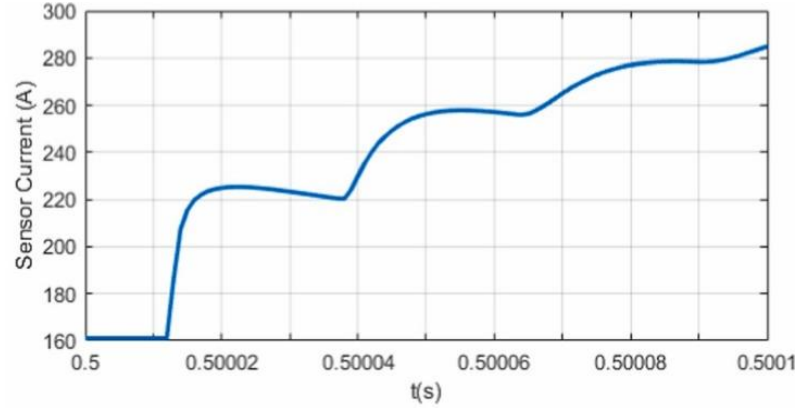
(a)
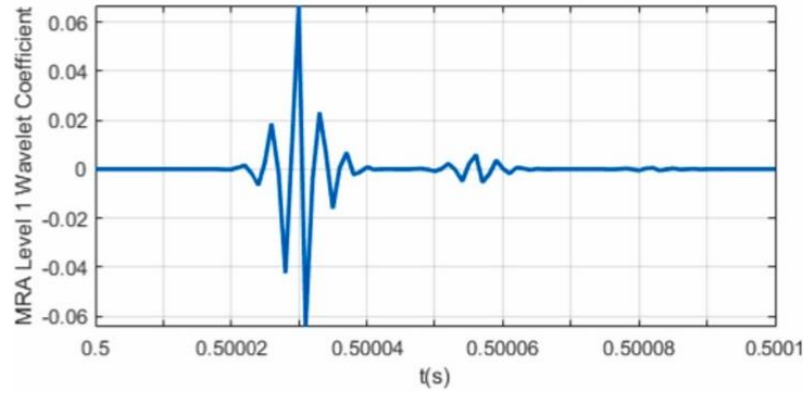
(b)
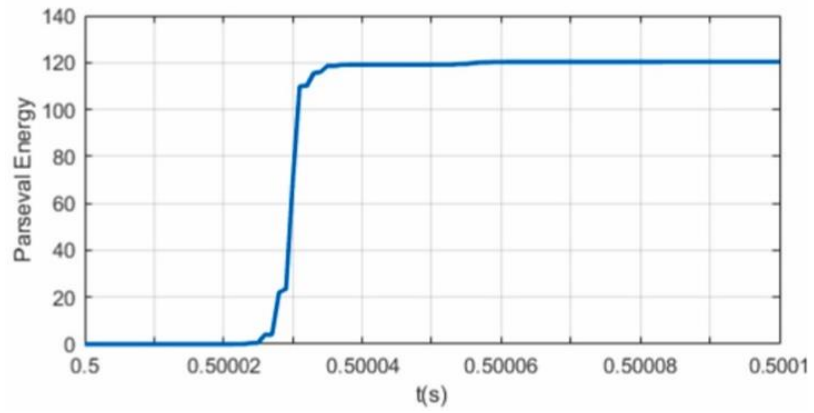
(c)

Figure 4. PP fault signatures for a fault at 2625 m in Fig. 2: (a) sensor fault current on the positive pole; (b) MRA's level 1 wavelet coefficient; (c) Parseval energy calculated from the wavelet coefficients.

15

As mentioned in Section 3, MRA is an effective tool to demonstrate the high-frequency fault signatures in different frequency ranges. In order to show how the Parseval energy calculated from the wavelet coefficients of each MRA's level is impacted for different fault locations, PP faults are applied at every 75 m of Cable C1 in Fig. 2. First, it is assumed that DWT's sampling frequency is 1 MHz. The Parseval energy values for three levels of MRA applied to the current measured at the sensor in Fig. 2 are shown in Fig. 5. Herein, level 1, 2, and 3 are associated with [250 kHz, 500 kHz], [125 kHz, 250 kHz], and [67.5 kHz, 125 kHz] frequency ranges. As seen in Fig. 5a, the Parseval energy value is generally decreasing as the fault location gets closer to the end of the cable, however, some local peaks are observed that happen at every 375 m. A similar pattern is observed in Fig. 5b; however, the local peaks occur at every 750–800 m. Finally, Fig. 5c shows that the local peaks occur at every 1500 m. As a rule of thumb, the number of local peaks approximately doubles from level 3 to level 2 and as well as from level 2 to level 1. In Fig. 6, it is assumed that the DWT's sampling frequency is 2 MHz. Doing so, level 1 and 2 are associated with [500 kHz, 1 MHz] and [250 kHz, 500 kHz] frequency ranges, respectively. As seen in Fig. 6, a similar pattern to Fig. 5 can be observed. In general, with a higher DWT's sampling frequency, (i) more oscillations on the Parseval energy profile of fault currents is observed, and (ii) the first incident of TW can be detected faster. The latter is based on an inherent feature of TWs in which the higher frequency TWs travel faster with a lower magnitude.

As discussed in Section 3, the spectrum of the energy of the fault signals corresponds to the Parseval energy calculated from the wavelet coefficients. The Parseval energy patterns for different fault locations in Fig. 5 and Fig. 6 are based on the inherent

16

behavior of TW currents and voltages as described in Section 2. More specifically, the incident TW current incurred by a fault can be formulated as

$$i^+(x,t) = |I_0^+|e^{-\alpha x}\cos(\omega t - \beta x), \tag{9}$$

where α and β denote the attenuation constant and phase constant, respectively, x denotes the distance from the fault location. Alternatively, one can formulate a function between the incident TW current at the cable terminal where the sensor is located (see Fig.2) and fault location assuming sliding faults along the cable. Doing so, the incident TW current at the cable terminal and the fault location, x_f, can be represented as

$$i^+(x_f,t) = |I_0^+|e^{-\alpha x_f}\cos(\omega t - \beta x_f). \tag{10}$$

According to (10), the relationship between the incident TW current at the sensor location and fault location inherits a combined exponential/sinusoidal behavior. Due to the existence of a cosine function, some local peaks are observed. These local peaks at a specific time t_1 occur at

$$x_{LocalPeak} = \frac{(\omega t_1 - 2n\pi)}{\beta}, n = 0,1,.... \tag{11}$$

Since the MRA coefficients correspond to the magnitude of TW at a specific frequency range and Parseval energy sums up the square of MRA coefficients over time, the Parseval energy as a function of fault location results in the waveshapes seen in Fig. 5 and Fig. 6. Moreover, from (11), the local peaks of incident TW current at the sensor location as a function of fault location occur periodically and are a function of TW angular frequency ω. According to (3) and (4), β also corresponds to ω. With ω appearing in the denominator of (11), one can conclude that as ω increases, more local peaks with a higher frequency can occur as seen in Fig. 5 and Fig. 6.
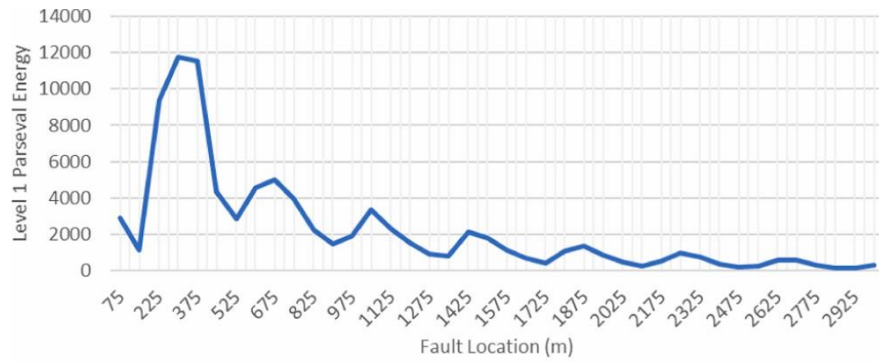
(a)
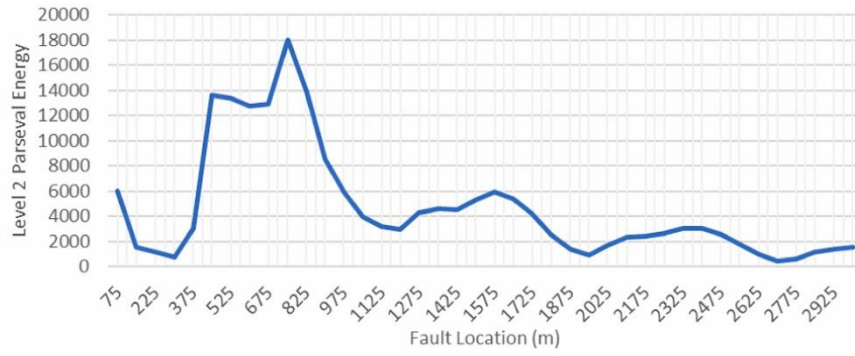
(b)
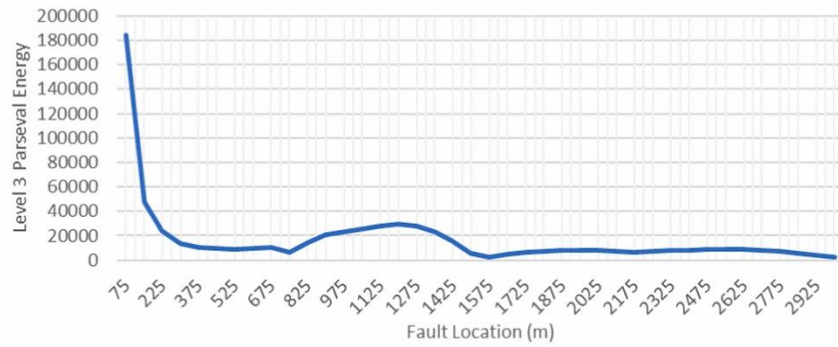
(c)

Figure 5. Parseval energy values for different fault locations on the cable of DC system with 1 MHz sampling frequency in Fig. 2: (a) MRA's level 1; (b) MRA's level 2; (c) MRA's level 3.
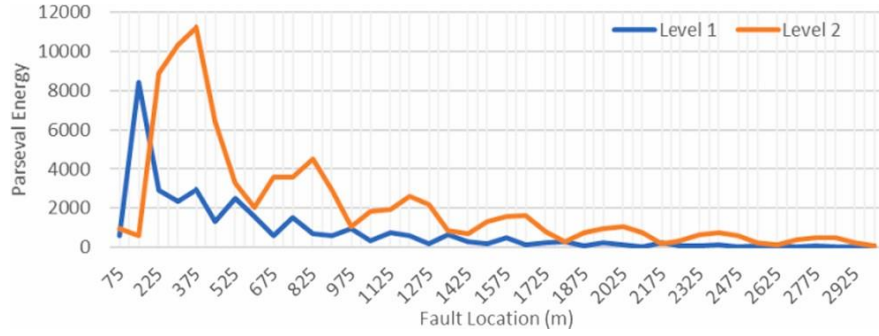
Figure 6. Parseval energy values for different fault locations on the cable of DC system with 2 MHz sampling frequency.

4.3. Pole to Ground Fault Characteristics

When a Pole to Ground (PG) fault occurs on a cable, the main converter of the DC microgrid is able to regulate the PP voltage and maintain it at the nominal voltage of the microgrid. After the PG fault occurs, at the fault location, the faulted pole's voltage is forced to zero, while the healthy pole voltage absolute value is forced to DC microgrid's nominal voltage. Therefore, the PP voltage and current measurements at the local terminal of cable (i.e. where the sensor is located) do not experience any significant change and only small transients are noticed on these quantities. The voltage and current at the sensor of DC microgrid in Fig. 2 for a PG fault at 1500 m are shown in Fig. 7. It should be noted that the microgrid's grounding happens at the middle point of the DC link of the microgrid's AC/DC converter. As seen in Fig. 7a and Fig. 7b, after the PG fault is applied at 0.25 s, only small transients are observed in the current and PP voltage at the sensor location. However, Fig. 7c and Fig. 7d show that the positive pole to ground (PPG) voltage drops to zero while the negative pole to ground (NPG) voltage reaches to − 750 V.

One distinguishing factor between PP and PG faults is how the Parseval energy of TWs for PP and PG voltage values change. For PG faults, positive and negative pole

19

voltages' Parseval energies experience a significantly higher change compared to PP

voltage's Parseval energies (See Fig. 8 and Fig. 9).
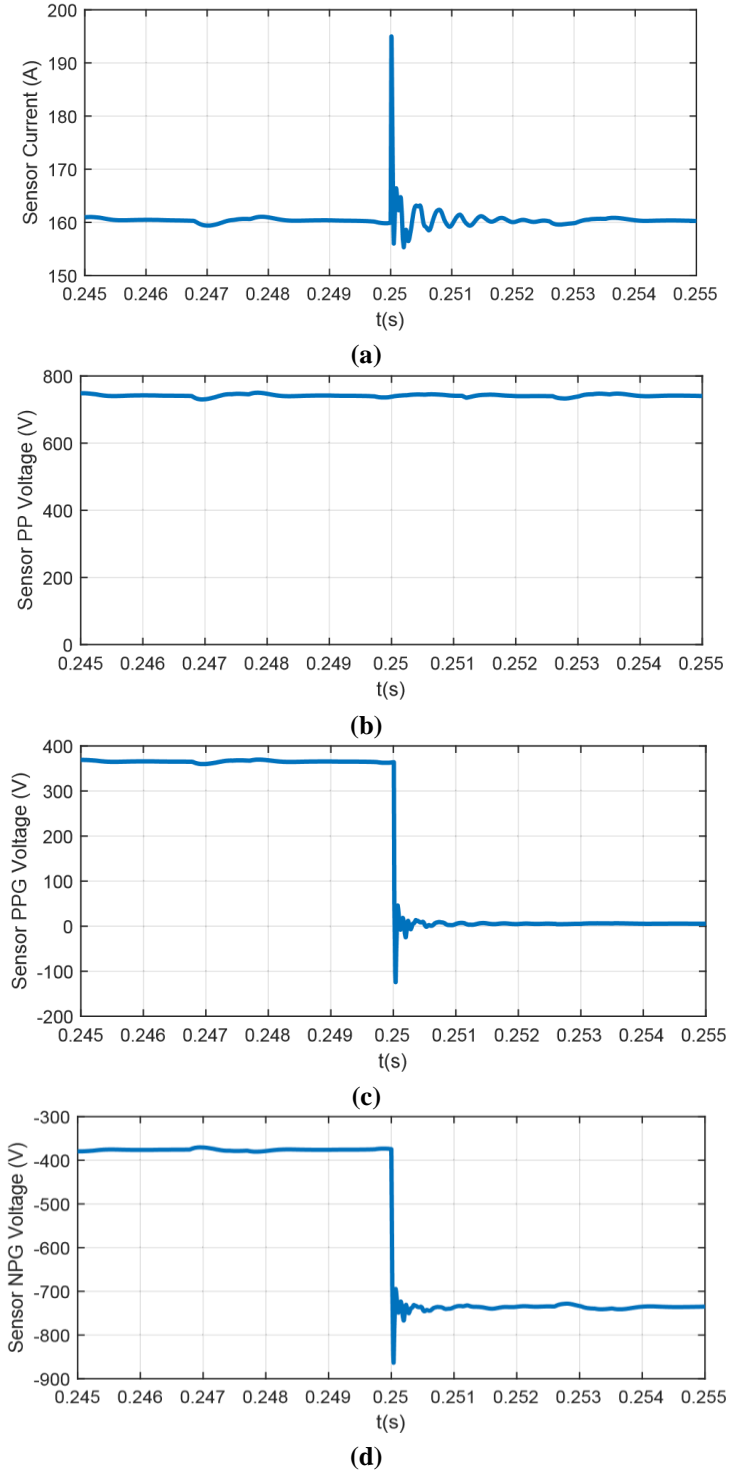
Figure 7. PG fault signatures for a fault at 1500 m in Fig. 2: (a) sensor fault current on positive pole; (b) PP voltage; (c) PPG voltage; (d) NPG voltage.
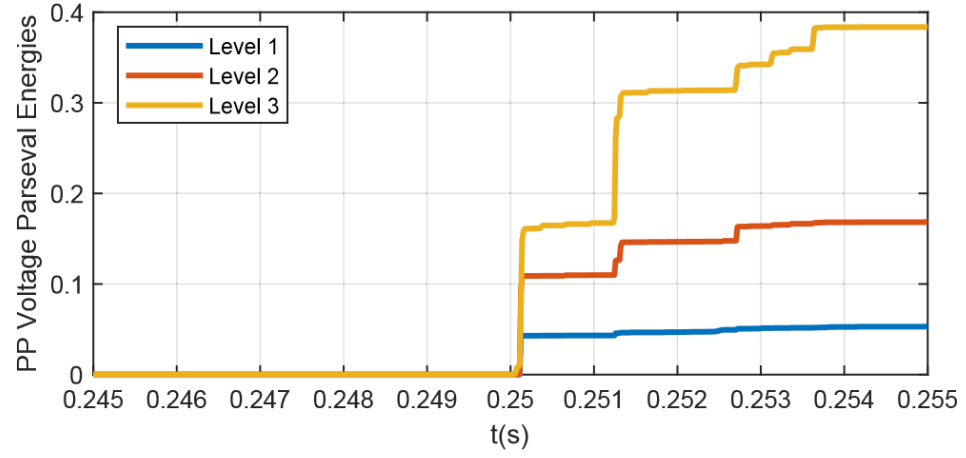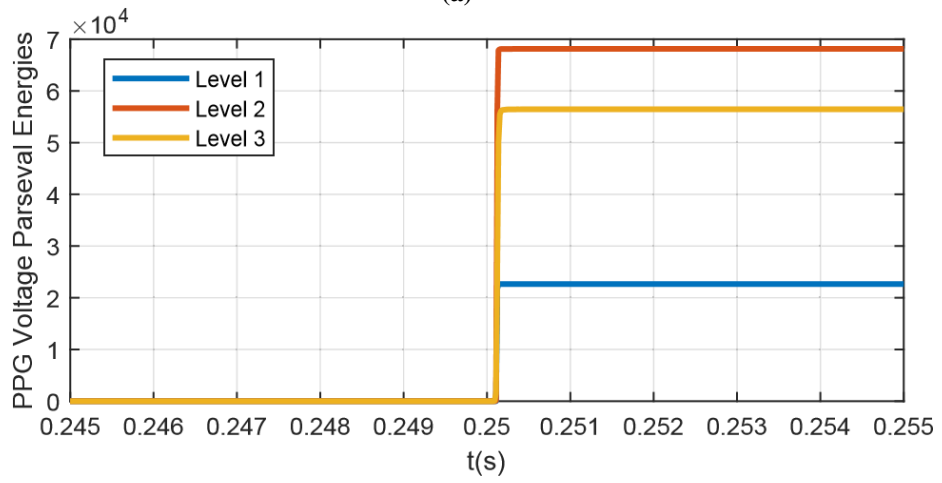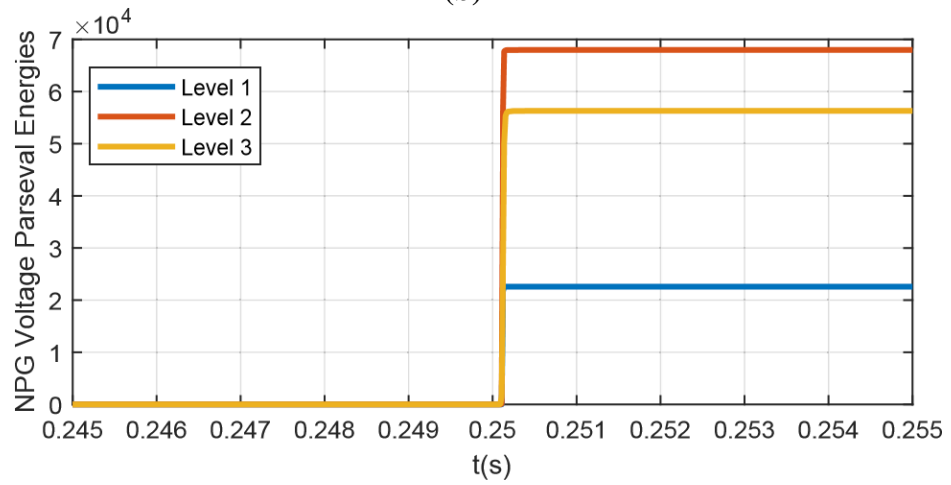
Figure 8. Impact of PG fault on pole to pole and pole to ground voltages' s Parseval energy: (a) PP voltage; (b) PPG voltage; (c) NPG voltage.

21
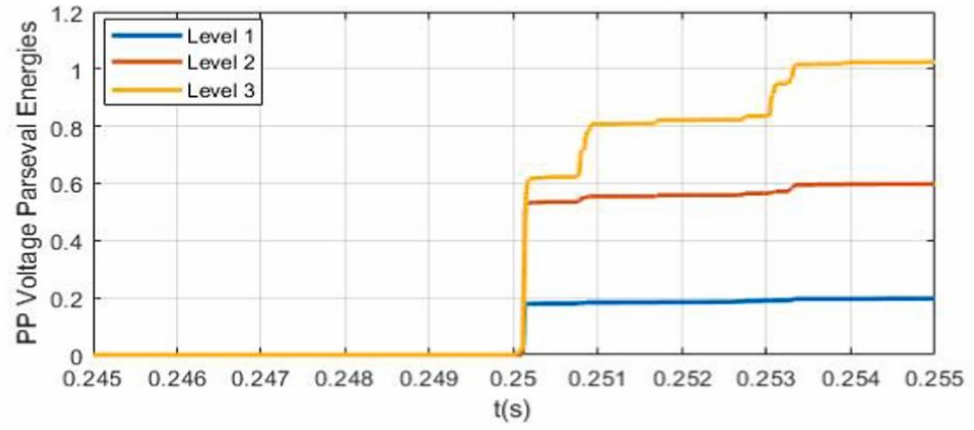
(a)
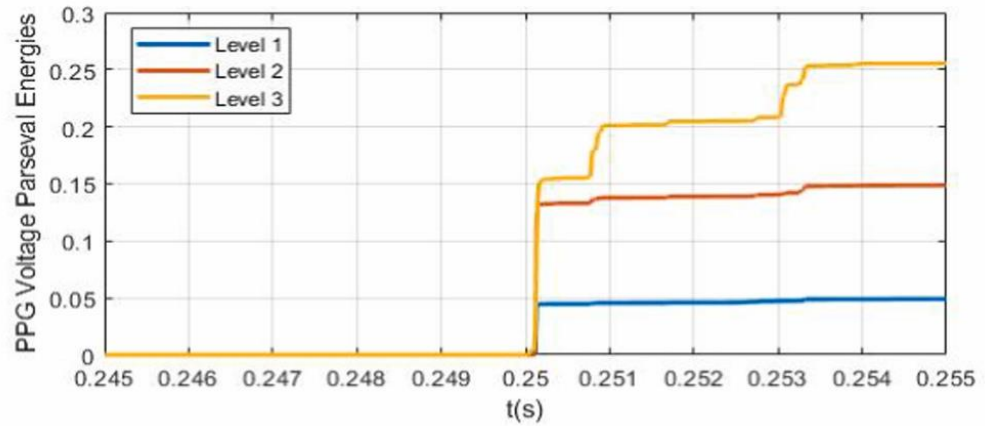
(b)
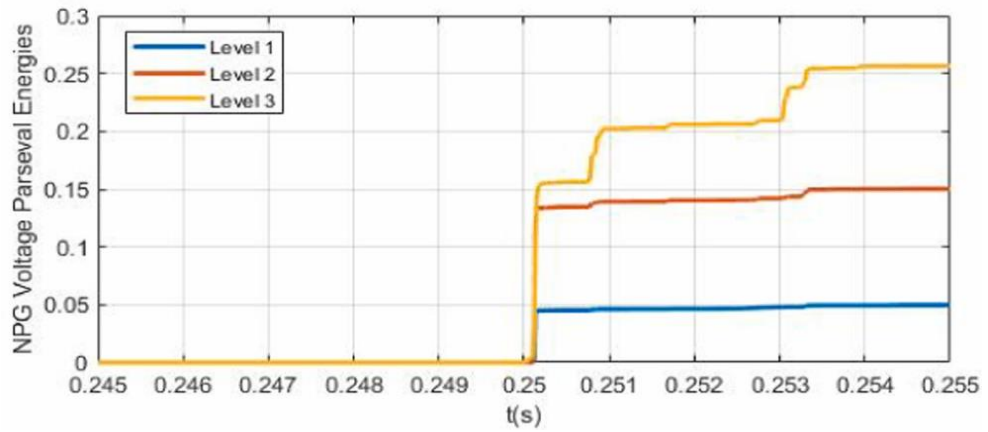
(c)

Figure 9. Impact of PP fault on pole to pole and pole to ground voltages' Parseval energy: (a) PP voltage; (b) PPG voltage; (c) NPG voltage.

22

5. Fault Classification and Location Scheme

5.1. Fault Detection and Direction Algorithm

In this section, the fault detection and direction, the fault classification, and the fault location algorithms are elaborated in detail. There are two classifications of faults that this section references much: the bolted (non-resistive) and unbolted (resistive) faults. The difference between the two is that the bolted fault can be thought of as the two faulted cables (pole-to-pole or pole-to-ground) being "bolted" together to essentially form a short circuit. The circuit is not truly non-resistive but very close, it is still subject to the small amount internal resistance of the system. The resistive (unbolted) fault is one that has some resistance between the two faulted cables in question, such as through electrical arcing. The resistive faults have a much lower fault current than bolted faults, which carry the maximum. The fault detection and direction algorithms will now be explained. The goal of the fault detection algorithm is to distinguish a fault scenario from a regular transient in the microgrid system. The fault detection algorithm is based on comparing the calculated Parseval energy value of the current flowing through the protection relay sensor, $E_{PRS,I}$, and a threshold η which is calculated as follows:

$$\eta = \gamma \, min(E_{PRS,I,PP}, E_{PRS,I,PG}), \tag{12}$$

where $E_{PRS,I,PP}$ and $E_{PRS,I,PG}$ are the summation of the first N levels of Parseval energy of the current flowing through the protection relay sensor for remote end bolted PP and PG faults, respectively, γ is a parameter to account for measurement noises. In general, regular microgrid transients (e.g., load outage, converter outage, etc.) create TWs with lower Parseval energy values compared to a bolted fault scenario. Therefore, η can be used to distinguish between a bolted fault scenario and other transients in the system. For highly

resistive faults, η may fail to distinguish a transient condition from the fault condition since resistive faults have lower current Parseval energy values. To tackle this challenge, the summation of the first N levels of Parseval energy of the PP, PPG, and NPG voltages are utilized. For a regular transient in the system, the Parseval energy values of PP, PPG, and NPG voltages remain very small. However, for a resistive PP fault, the summation of the first N levels of Parseval energy of PP voltage is much higher than a regular transient. For a resistive PG fault, the summation of the first N levels of Parseval energy of PPG and NPG voltages are much higher than the regular transients. Therefore, by calculating the Parseval energy values of PP, PPG, and NPG voltage values, one can distinguish between a regular transient and highly resistive fault condition.

The fault direction algorithm is extracted from [18]. The algorithm assumes that the convention for the direction of current measurement units is as follows (See Figure 10): on the positive pole, the positive direction of the current measurement unit is toward the line while on the negative pole, the positive direction of the current measurement unit is toward the terminal. Depending on the fault type and location, one of the following scenarios can happen:

- For PP faults, when a forward fault is applied in front of the measurement unit, the measurement unit will see a decreasing voltage surge and an increasing current surge.
- For PP faults, when a forward fault is applied behind the measurement unit, the measurement unit will see a decreasing voltage surge and a decreasing current surge.
- For PG faults, since the changes of the measured current at the relay location are minimal, it is recommended to use the fault location algorithm in Section 5.3. If the fault is located on one of the cables behind the measurement unit, the amount of Parseval

energy values seen at the relay location are highly attenuated due to the reflections at the local terminal.
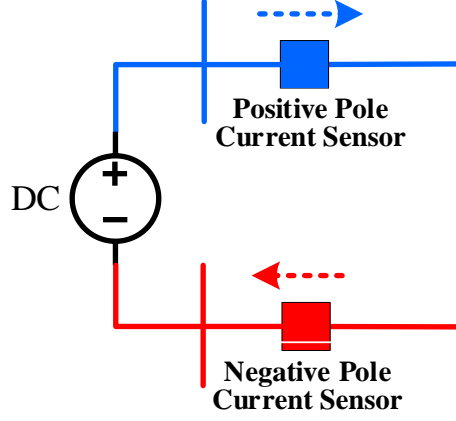
Figure 100. Convention for fault direction algorithm.

5.2. Fault Classification Algorithm

To distinguish between PP and PG faults, the Parseval energy of PP voltage at the sensor location is compared against the Parseval energies of the positive or negative pole to ground voltage. This procedure is shown in Fig. 11. As discussed in Section 4, for PG faults, the Parseval energies of positive or negative pole to ground voltage are significantly higher than the Parseval energy of PP voltage. To this end, the algorithm first calculates the summation of the first N levels of Parseval energy values related to PP voltage and PPG voltage using (i.e., $E_{PRS,VPP}$ and $E_{PRS,VPG}$, respectively). Then, $E_{PRS,VPP}$ and $E_{PRS,VPG}$ are compared against each other to determine the fault type. Herein, the ratio of $E_{PRS,VPG}$ /$E_{PRS,VPP}$ is calculated and compared against λ_{FT} threshold. This threshold can be found by trial and error on the microgrid system. Since $E_{PRS,VPG}$ is significantly higher than $E_{PRS,VPP}$ for PG faults, λ_{FT} is always greater than 1. As a rule of thumb, the threshold is selected at around 10% of the $E_{PRS,VPG}$ /$E_{PRS,VPP}$ ratio for the remote end PP and PG faults.

Once the fault type (i.e., PP versus PG) is identified, an SVM classifier is used to find if the fault is resistive or bolted. SVM has been proven to be a very effective as a classification tool. The preliminaries of SVM are discussed in [56]. For this purpose, multiple bolted and resistive faults are simulated at different locations of cable (e.g., every 25 m) in a simulation software package (e.g., PSCAD/EMTDC). It should be noted that the fault resistance values adopted in the simulations depend on the DC microgrid conditions like voltage level or geographical location. After the simulation results are gathered, the SVM classifier is trained using the labeled Parseval energy values. For PP faults, the inputs to the SVM classifier are the N level Parseval energy values of pole current and PP voltage at the sensor location. For PG faults, the inputs to the SVM classifier are the N level Parseval energy values of pole current and PPG voltage at the sensor location. The output of the classifier is the type of fault, bolted or resistive. Matlab was utilized with the "fitcsvm" function for classification, the training inputs and outputs were described above. For more information on using the "fitcsvm" function, see [57].
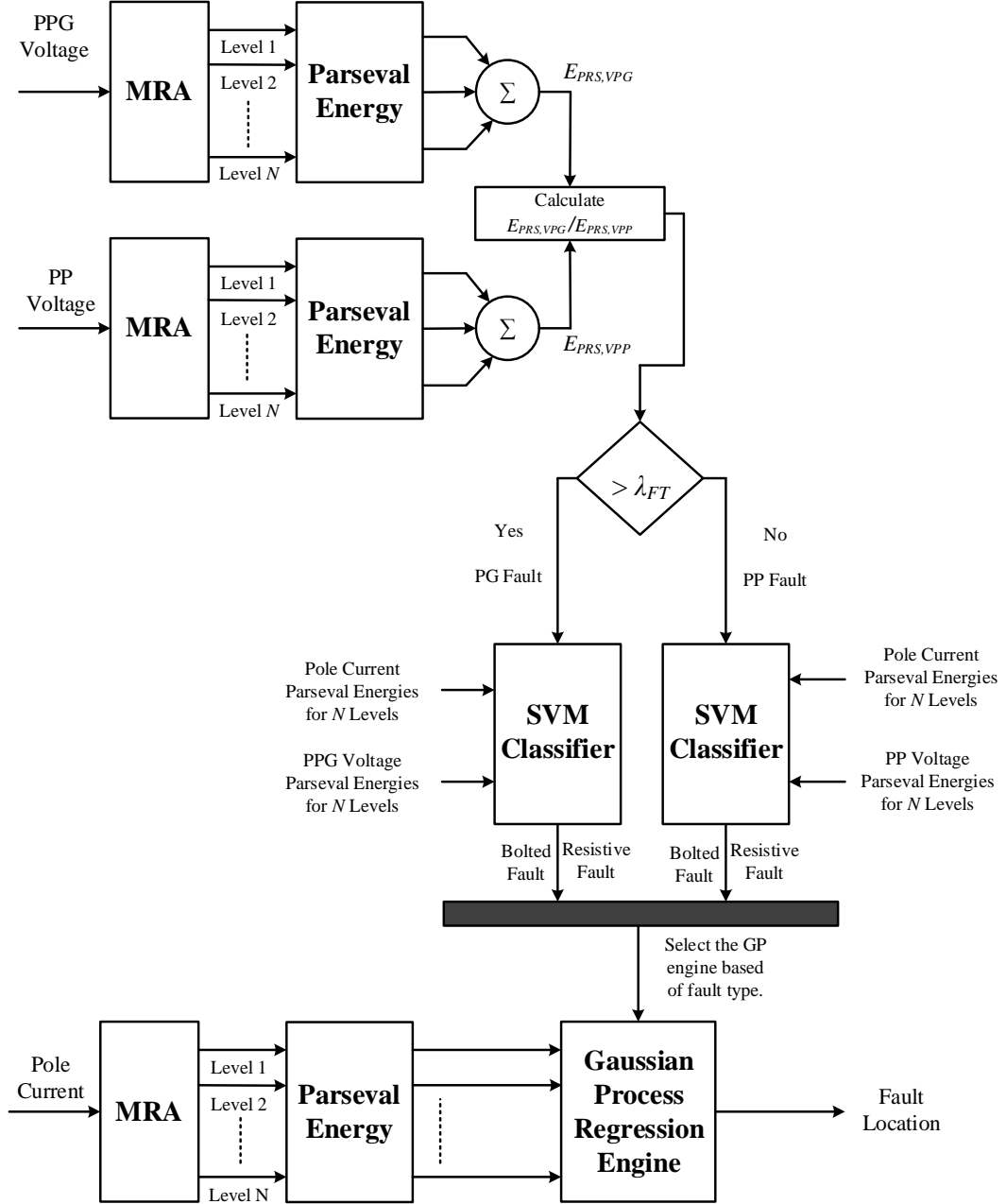
Figure 111. Fault classification and location algorithm.

5.3. Fault Location Algorithm

Once the fault type is classified, the proposed approach ensures that the fault is located on the primary cable. To this end, the Parseval energy value of the current flowing

through the protection relay sensor, $E_{PRS,I}$, is calculated. Depending on the fault type, $E_{PRS,I}$ is compared against the precalculated Parseval energy value related to the remote end bolted PP, resistive PP, bolted PG, or resistive PG fault. The proposed fault location algorithm relies on the Parseval energy values gathered from MRA. The algorithm utilizes the first N levels of MRA, calculates the Parseval energy of the first TW incidents, and then utilizes GP regression engines to find the fault location. The proposed fault location algorithm is shown in Fig. 10.

GP Regression: A GP is a generalization of the Gaussian probability distribution. GP is a collection of any finite number of random variables with a joint Gaussian distribution. GP is a very effective tool for classification and regression of datasets with linear or nonlinear relationships. A training set of n observations (inputs and outputs) is given by $\mathbf{D} = \{(x_i, y_i)|i = 1,\ldots,n\}$ or equivalently $\mathbf{D} = (X, \mathbf{y})$. A GP regression model predicts an output value y_{new} for the new input of $\mathbf{x}_{new}$. A linear GP regression model can be written as [58]

$$y = \mathbf{x}^T \beta + \varepsilon, \tag{13}$$

where $\varepsilon \sim N\left(0, \sigma_n^2\right)$ denotes an additive noise described by a Gaussian distribution with zero mean and variance of σ^2_n. The regression tool tries to estimate the coefficients β and variance σ^2_n. A GP regression tool finds the solution by incorporating the GP-based latent variables $\{f(\mathbf{x}_i)|i = 1, \ldots, n\}$ and the basis functions h, which lead to the formation of

$$y = h(\mathbf{x})^T \beta + f(\mathbf{x}), \tag{14}$$

with $f(\mathbf{x})$ formed by GP with zero mean and covariance function of $k(\mathbf{x}, \mathbf{x}')$. A sample of solution y can be represented as

$$P(y_i|f(\boldsymbol{x}_i), \boldsymbol{x}_i) \sim N(y_i|h(\boldsymbol{x}_i)^T \beta + f(\boldsymbol{x}_i), \sigma^2). \tag{15}$$

Equivalently, the joint distribution of latent variables in the probabilistic GP regression model is

$$P(f|X) \sim N(f|0, K(X, X')), \tag{16}$$

where $X = [\boldsymbol{x}_1^T \quad \boldsymbol{x}_2^T \quad \dots \quad \boldsymbol{x}_n^T]$ and

$$K(X, X') = \begin{bmatrix} k(\boldsymbol{x}_1, \boldsymbol{x}_1) & k(\boldsymbol{x}_1, \boldsymbol{x}_2) & \cdots & k(\boldsymbol{x}_1, \boldsymbol{x}_n) \\ k(\boldsymbol{x}_1, \boldsymbol{x}_2) & k(\boldsymbol{x}_2, \boldsymbol{x}_2) & \cdots & k(\boldsymbol{x}_2, \boldsymbol{x}_n) \\ \vdots & \vdots & \vdots & \vdots \\ k(\boldsymbol{x}_n, \boldsymbol{x}_1) & k(\boldsymbol{x}_n, \boldsymbol{x}_2) & \cdots & k(\boldsymbol{x}_n, \boldsymbol{x}_n) \end{bmatrix}. \tag{17}$$

The covariance functions are represented through a set of Kernel hyperparameters [58].

The fault location algorithm utilizes different GP regression engines corresponding to bolted and resistive PP and PG faults. In order to effectively train the GP regression engine, the number of MRA levels, *N*, requires to be greater than or equal to three. Although the higher value of *N* increases the accuracy of the GP regression engine, increasing the levels of MRA decreases the speed of the fault location algorithm as MRA has a slower response for lower frequency ranges. The value of Parseval energy selected for each decomposition level is the value that is observed after the first traveling wave corresponding to that decomposition level reaches the sensor location. In this thesis, to effectively train the GP regression engine, the Parseval energy of MRA's six levels at multiple fault locations (e.g., every 50 m of the cable) are utilized as the training inputs and outputs, respectively. Once trained, the GP regression tool can identify the fault location using the Parseval energy of MRA's six levels for any new fault scenario on the

cable. Both SVM and GP don't require extensive training datasets for their effective operations.

The Gaussian Process for Machine Learning (GPML) add on toolbox [58] for Matlab was utilized to formulate the machine learning algorithms. An exponential kernel function was chosen for the analysis. The training input and outputs were described above. For a comprehensive explanation of how to use the code, see [58].

Remark 1. In this thesis, six MRA's levels are used as the inputs to the GP regression engine. Generally, it is preferred to utilize more MRA's levels in order to cover more signatures of the fault current at a wider frequency range. However, with a higher MRA level, the computational time of the algorithm becomes significantly higher which in turn slows down the protection scheme [38,55]. Therefore, six levels of MRA are selected to provide a tradeoff between the comprehensiveness of fault current signatures and the computational efficiency of the algorithm.

Remark 2. It should be noted that the proposed protection scheme can effectively work with different DWT sampling frequencies. The DWT sampling frequency only impacts the speed of the fault location algorithm. With a higher sampling frequency, MRA is able to calculate the first N levels of wavelet coefficients faster. For example, with 8 MHz sampling frequency and six MRA levels, the proposed algorithm will be able to find the fault location in 200 µs. With the recent advancements in signal processing and measurement technologies, high-frequency data sampling and measurement can be easily accommodated for the implementation of the proposed scheme. In fact, existing commercial TW relays are able to perform very high frequency (in the order of MHz) measurements [59].

Remark 3. For both SVM classifier and GP regression tools, a supervised learning approach is adopted. The supervised learning uses the simulation model to create labeled data sets for training both SVM and GP tools. When the proposed protection scheme is deployed in the field, the data gathered from the fault incident is used to identify fault type and estimate fault location using the most recent trained SVM and GP tools. Then, the new dataset along with the fault type and location will be added to the training set and both SVM and GP tools will be trained with the updated training set.

Remark 4. Mother wavelet can significantly impact the accuracy and speed of the MRA. It is of particular importance to select a suitable mother wavelet for the proposed fault location algorithm. The criteria for selecting a mother wavelet are: (i) incorporating enough number of vanishing points for accounting for the salient features of waveforms, (ii) sharp cutoff frequencies to minimize the amount of energy leakage to the next decomposition level, and (iii) being orthonormal, (iv) minimum description length (MDL) [38,60]. According to [38], Daubechies (db) mother wavelets are promising candidates that comply with the aforementioned criteria and facilitate fast and accurate MRA.

Remark 5. The proposed protection approach can also provide backup protection for forward cables that are located in front of the protection relay. This is achieved by calculating the Parseval energy value related to faults applied at the remote end of the shortest forward cable. If the Parseval energy of the current flowing through the protection relay sensor is lower than the precalculated Parseval energy value of a fault applied at the remote end of the primary cable and greater than the Parseval energy value related to a fault applied at the remote end of the shortest forward cable, then the protection relay can provide backup protection. In order to coordinate backup and primary protection relays, the backup

protection should operate with a delay named the coordination time interval (CTI). According to [14], the CTI (i) should be greater than the operating time of primary protection relay, (ii) should be greater than the operating time of solid-state DC circuit breaker which is assumed to be around 200 µs, and (iii) must include a 20% security margin. For example, if the operating time of the primary relay is 200 µs, then the CTI is equal to $(200 + 200) \times 1.2 = 480$ µs.

6. Performance Verification

6.1. DC Microgrid 1

To verify the performance of the proposed fault detection and location scheme, two different DC microgrid systems are utilized. The simulation results for these two microgrid systems will be shown now, starting with Microgrid 1. The DC microgrid 1 test system is illustrated in Fig. 12. This DC microgrid system is based on a real DC microgrid system in the city of Albuquerque, NM. We have utilized high frequency (in the order of 10 MHz) field measurements from the actual microgrid to calibrate the created model in PSCAD/EMTDC. The DC microgrid is supplying four residential houses. Each residential house is described as a nanogrid (NG). Each NG included the residential house load, a PV system, a Battery Energy Storage System (BESS), and DC-DC converters to integrate NG into the rest of the microgrid. The PV system is associated with a maximum power tracking scheme. The size of the PV system in each NG is 10 kW while the size of BESS is 6 kW/12 kWh. The load of NG1, NG3, and NG4 is 56.25 kW and the load of NG2 is equal to 50 kW. It is assumed that the microgrid includes a community BESS and PV system with the size of 20 kW/40 kWh and 18 kW, respectively. The microgrid's main converter is modeled as a multi-level voltage sourced converter [61]. The microgrid's grounding happens at the middle point of the DC link of the microgrid's AC/DC converter. The size of this converter is 500 kW. Load L1′s size is 10 Ω. RC1 is 25 mΩ and LC1 is 20 μH. In Fig. 12, Relays R1 to R6 identify the location of our proposed fault detection and location algorithms. The cables configuration is provided in Fig. 3. It is assumed that each cable has its own local protection.

To verify the effectiveness of the proposed scheme, bolted and resistive PP and PG faults are applied at different locations of all six cables in the DC microgrid test system shown in Fig. 12. The fault resistance for both PP and PG faults is equal to 5 Ω. The length of each these simulations, DWT's sampling frequency is 8 MHz. Six levels of MRA are used for the fault classification and location algorithm. For Cables C1 and C6, 40 different fault locations are simulated; for Cables C2 and C5, 30 different fault locations are simulated; for Cable C3, 38 different fault locations are simulated; for Cable C4, 22 different fault locations are simulated. The captured Parseval energy values for bolted PP faults on Cables C1 to C6 are illustrated in Figs. 13–18.
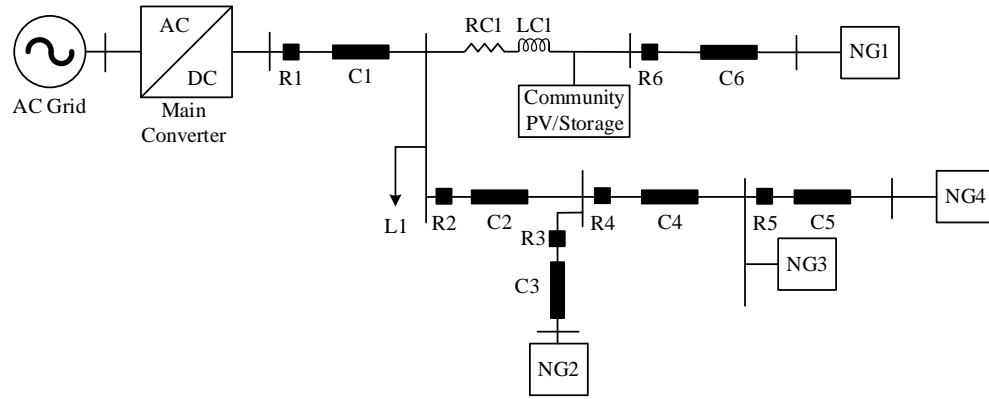

Figure 12. DC Microgrid 1.

*Table 1. Cable lengths and fault locations values.*

Cable	C1	C2	C3	C4	C5	C6
Length	2000 m	800 m	1000 m	600 m	800 m	2000 m
Fault locations	At every 50 m	50 m, 75 m, 100 m, 125 m, 150 m, 175 m, 200 m, 225 m, 250 m, 275 m, 300 m, 325 m, 350 m, 375 m, 400 m, 425 m, 450 m, 475 m, 500 m, 525 m, 550 m, 575 m, 600 m, 625 m, 650 m, 675 m, 700 m, 725 m, 750 m, 800 m	50 m, 75 m, 100 m, 125 m, 150 m, 175 m, 200 m, 225 m, 250 m, 275 m, 300 m, 325 m, 350 m, 375 m, 400 m, 425 m, 450 m, 475 m, 500 m, 525 m, 550 m, 575 m, 600 m, 625 m, 650 m, 675 m, 700 m, 725 m, 750 m, 775 m, 800 m, 825 m, 850 m, 875 m, 900 m, 925 m, 950 m, 1000 m	50 m, 75 m, 100 m, 125 m, 150 m, 175 m, 200 m, 225 m, 250 m, 275 m, 300 m, 325 m, 350 m, 375 m, 400 m, 425 m, 450 m, 475 m, 500 m, 525 m, 550 m, 600 m	50 m, 75 m, 100 m, 125 m, 150 m, 175 m, 200 m, 225 m, 250 m, 275 m, 300 m, 325 m, 350 m, 375 m, 400 m, 425 m, 450 m, 475 m, 500 m, 525 m, 550 m, 575 m, 600 m, 625 m, 650 m, 675 m, 700 m, 725 m, 750 m, 800 m	At every 50 m
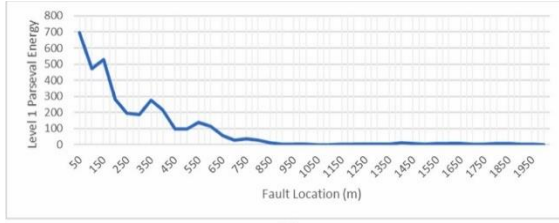
(a)

(b)
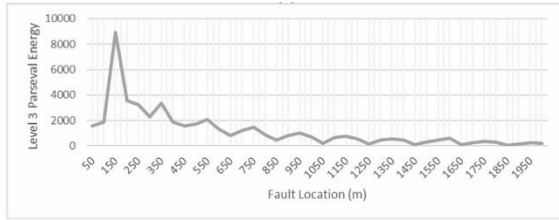
(c)

(d)

(e)

(f)

Figure 13. Parseval energy values for bolted PP faults on C1: (a) Level 1; (b) Level 2; (c) Level 3; (d) Level 4; (e) Level 5; (f) Level 6.
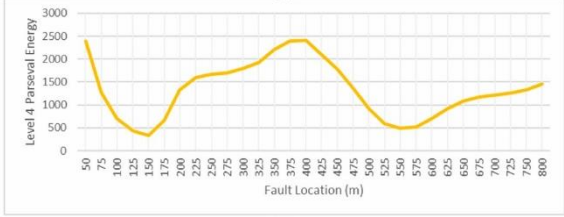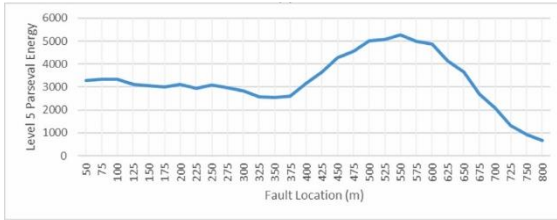
Figure 14. Parseval energy values for bolted PP faults on C2: (a) Level 1; (b) Level 2; (c) Level 3; (d) Level 4; (e) Level 5; (f) Level 6.
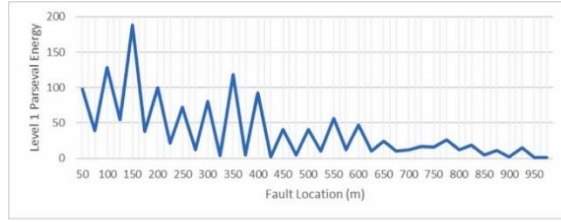
(a)
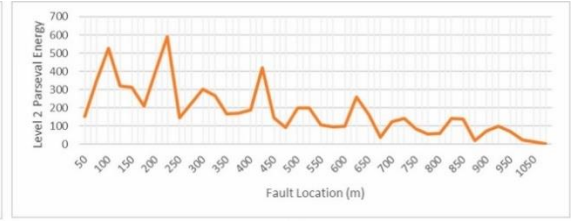
(b)
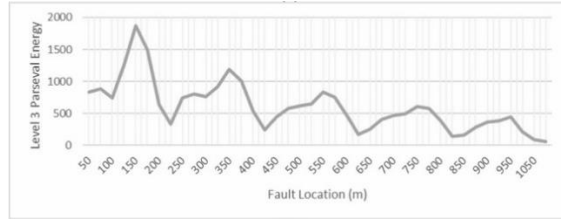
(c)
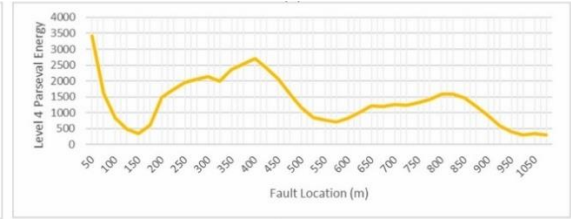
(d)
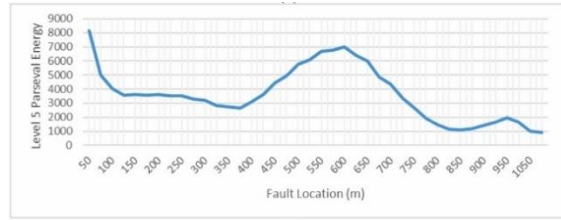
(e)
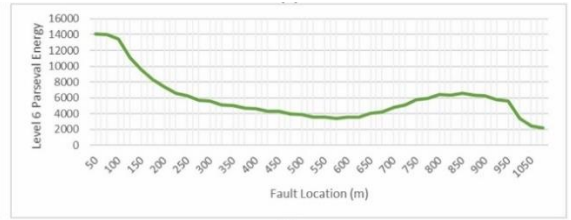
(f)

Figure 15. Parseval energy values for bolted PP faults on C3: (a) Level 1; (b) Level 2; (c) Level 3; (d) Level 4; (e) Level 5; (f) Level 6.
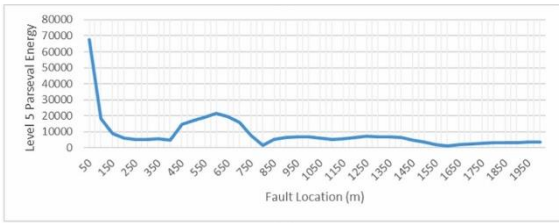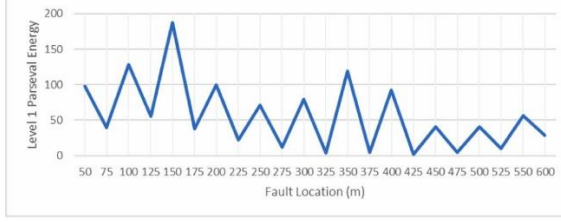
(a)
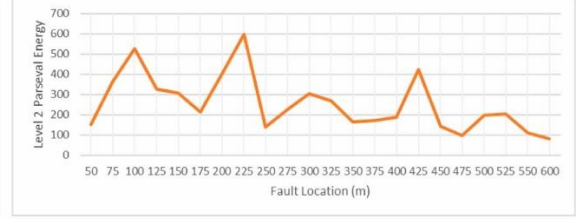
(b)
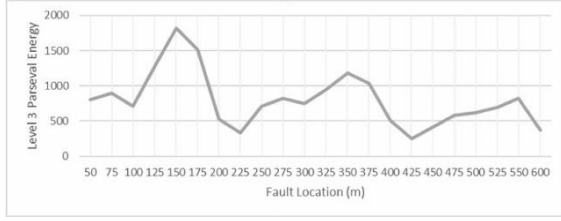
(c)
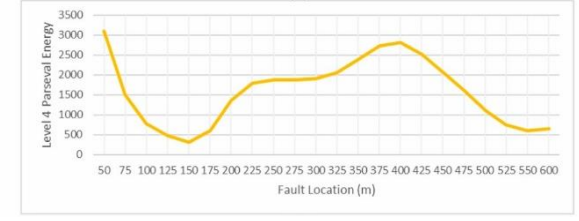
(d)
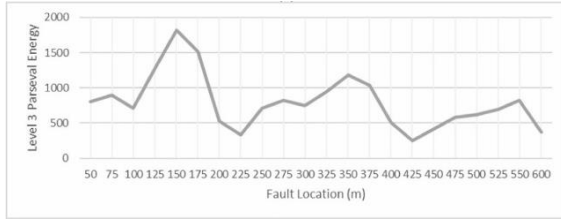
(e)
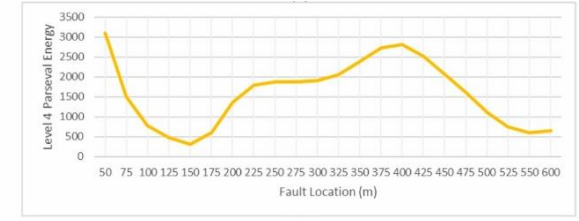
(f)

Figure 16. Parseval energy values for bolted PP faults on C4: (a) Level 1; (b) Level 2; (c) Level 3; (d)
Level 4; (e) Level 5; (f) Level 6.
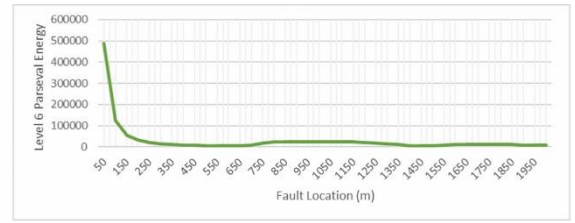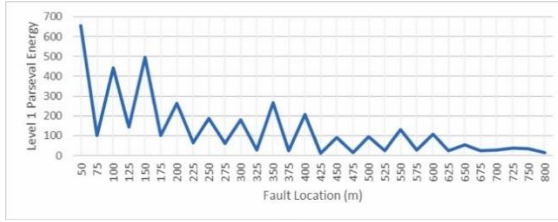
(a)

(b)

(c)

(d)
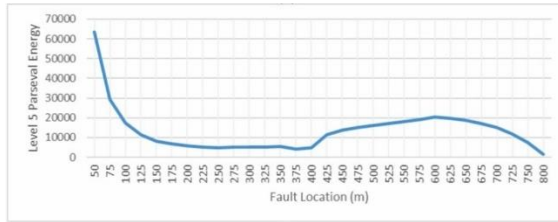
(e)
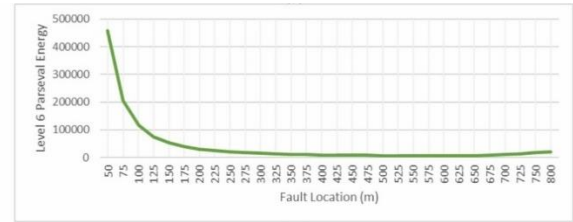
(f)

Figure 17. Parseval energy values for bolted PP faults on C5: (a) Level 1; (b) Level 2; (c) Level 3; (d) Level 4; (e) Level 5; (f) Level 6.
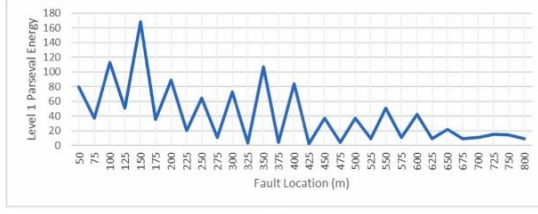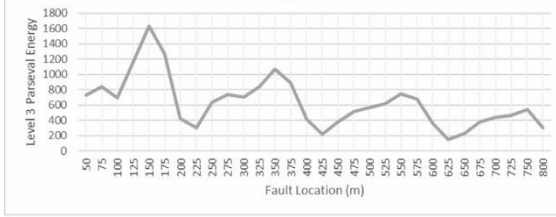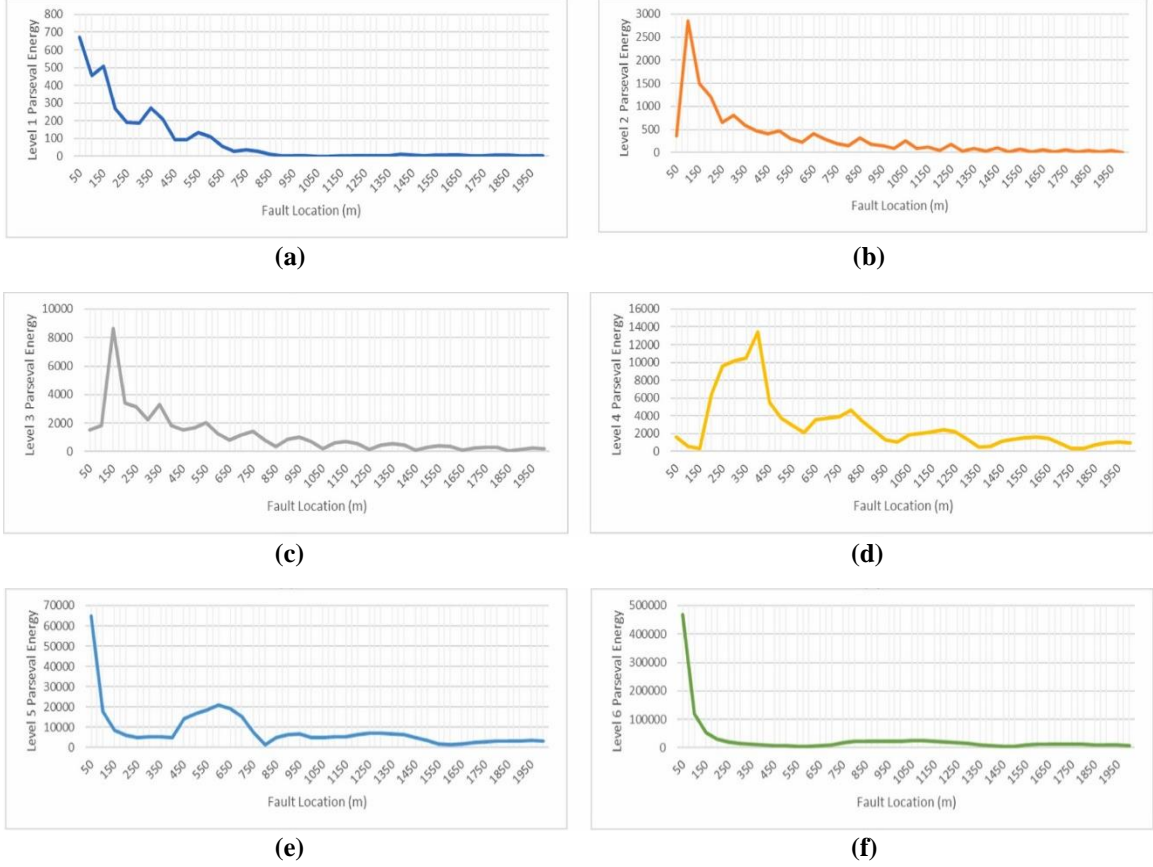
Figure 18. Parseval energy values for bolted PP faults on C6: (a) Level 1; (b) Level 2; (c) Level 3; (d) Level 4; (e) Level 5; (f) Level 6.

In Table 2, the Parseval energy values measured at Relays R2, R3, R4, R5, and R6 for the remote end faults on Cables C2, C3, C4, C5, and C6 are compared against the Parseval energy values resulting from non-fault transient events close to each relay. The non-fault transients include the outage of a cable or NG as well as nonlinear load switching inside NGs. For the nonlinear load switching scenarios, it is assumed that all the loads are modeled as a nonlinear voltage-dependent model where the load's power is a nonlinear function voltage satisfying $P = P_0(V/V_0)^2$ with P and V as the load's power and operating voltage and P_0 and V_0 as the rated power and voltage of load. For each cable, the close- by nonlinear load is switched off. All transients occur at 2.5 sec and then the Parseval energy

values of the relay's current are captured after 200 us, which are summarized in Table 2. As seen, the non-fault transients result in much lower Parseval energy values on current TWs captured at Relays R2, R3, R4, R5, and R6.

Table 2. Comparison of faults' Parseval energy values versus a regular transients' Parseval energy values.

Relay	Scenario	Level 1	Level 2	Level 3	Level 4	Level 5	Level 6
R2	Remote bolted PP fault on C2	8.87	47.22	300	1459	670	9037
	Remote resistive PP fault on C2	2.15	11.51	72.59	393	145	2871
	Remote bolted PG fault on C2	8.864	47.11	297.9	1461	668.3	8722
	Remote resistive PG fault on C2	0.93	4.96	30.5	161	71.5	1365
	C3 Outage	1.43×10^{-11}	6.6×10^{-10}	8.15×10^{-09}	1.99×10^{-07}	4.25×10^{-06}	2.61×10^{-05}
	NG2's Load Switching	2.67×10^{-9}	4.75×10^{-8}	5.92×10^{-7}	6.63×10^{-7}	1.96×10^{-6}	1.4×10^{-5}
R3	Remote bolted PP fault on C3	0.6	23.65	212	305	1641	3404
	Remote resistive PP fault on C3	8.54×10^{-7}	3.35×10^{-5}	0.0003	0.00043	0.0023	0.0049
	Remote bolted PG fault on C3	0.8951	33.61	291.8	425.7	2389	6870
	Remote resistive PG fault on C3	0.16	5.89	50.01	79.69	410	1044
	NG2 Outage	4.8×10^{-10}	2.18×10^{-09}	8.73×10^{-09}	5.25×10^{-08}	5.74×10^{-06}	6.25×10^{-05}
	NG2's Load Switching	1.47×10^{-9}	3.45×10^{-8}	9.87×10^{-8}	2.07×10^{-7}	6.43×10^{-7}	6×10^{-6}
R4	Remote bolted PP fault on C4	29.05	79.7	372	648	4423	5469
	Remote resistive PP fault on C4	3×10^{-4}	8×10^{-4}	3.7×10^{-3}	6.5×10^{-3}	0.044	0.055
	Remote bolted PG fault on C4	29.97	87.73	396.2	705.6	5538	4348
	Remote resistive PG fault on C4	2.03	6.33	29.56	60.55	454	389
	NG3 Outage	1.23×10^{-12}	3.12×10^{-11}	6.41×10^{-10}	4.47×10^{-08}	7.64×10^{-07}	3.95×10^{-6}
	NG3's Load Switching	1.05×10^{-10}	7.49×10^{-9}	4.94×10^{-8}	1.83×10^{-7}	5.06×10^{-6}	2.76×10^{-5}
R5	Remote bolted PP fault on C5	15.98	104	782	3895	1343	20367
	Remote resistive PP fault on C5	0.00017	0.0011	0.0084	0.0418	0.0144	0.218
	Remote bolted PG fault on C5	5.813	32.60	207.5	925.7	1088	3838
	Remote resistive PG fault on C5	0.92	5.29	35.46	169	167	696
	NG4 Outage	6.96×10^{-13}	2.07×10^{-11}	1.3×10^{-10}	1.49×10^{-09}	1.21×10^{-07}	1.09×10^{-7}
	NG4's Load Switching	6.52×10^{-13}	2.04×10^{-11}	1.32×10^{-10}	1.49×10^{-9}	1.18×10^{-7}	1.12×10^{-7}
R6	Remote bolted PP fault on C6	1.76	6.05	182	949	3276	7350
	Remote resistive PP fault on C6	1.72×10^{-5}	6.46×10^{-5}	0.0019	0.0104	0.035	0.079
	Remote bolted PG fault on C6	0.0006	0.06203	0.5678	8.558	311.13	3699
	Remote resistive PG fault on C6	9.31×10^{-5}	0.01	0.1	1.44	54.38	722
	NG1 Outage	6.56×10^{-12}	7.8×10^{-12}	1.46×10^{-10}	1.12×10^{-09}	1.11×10^{-08}	2.16×10^{-07}
	NG1's Load Switching	4.14×10^{-12}	2.27×10^{-11}	7.68×10^{-11}	7.44×10^{-10}	9.59×10^{-9}	2.21×10^{-7}

The algorithm was able to effectively distinguish PP faults from PG ones by selecting 10 as the λ_{FT} threshold in Fig. 10. To verify the performance of the SVM classifier for identifying bolted faults from resistive ones, two separate datasets were used for training and testing. 60% of the available data were used for training and 40% of them were used for testing randomly. In the SVM, a linear Kernel is used while the penalty factor for misclassified data is set to 1. The verification results rendered 100% precision in classifying bolted faults versus resistive faults using the six levels of current and voltage Parseval energies at Cable C1. In Table 3, the fault location estimation errors using GP engines for all cables and different types of faults are summarized. The estimation error percentage is equal to the mean absolute error of testing dataset over the length of the cable. For each cable, around 65% of the gathered datasets are used for training and the rest are used for testing. The training and testing datasets are selected randomly. The fault location estimation errors in Table 3 verify the effectiveness of the proposed fault location algorithm. In Table 3, the estimation error depends on the number of datasets available for training and the length of the cable. In general, simulating faults at more locations can increase the number of training datasets which in turn improves the performance of the GP regression engine in estimating fault location. The regression results for Cable C4 are illustrated in Fig. 19. As seen, for both resistive and bolted PP and PG faults, the GP regression engine can effectively locate faults with small estimation errors. In all cases, the proposed algorithm is able to find the fault location in 200 µs.
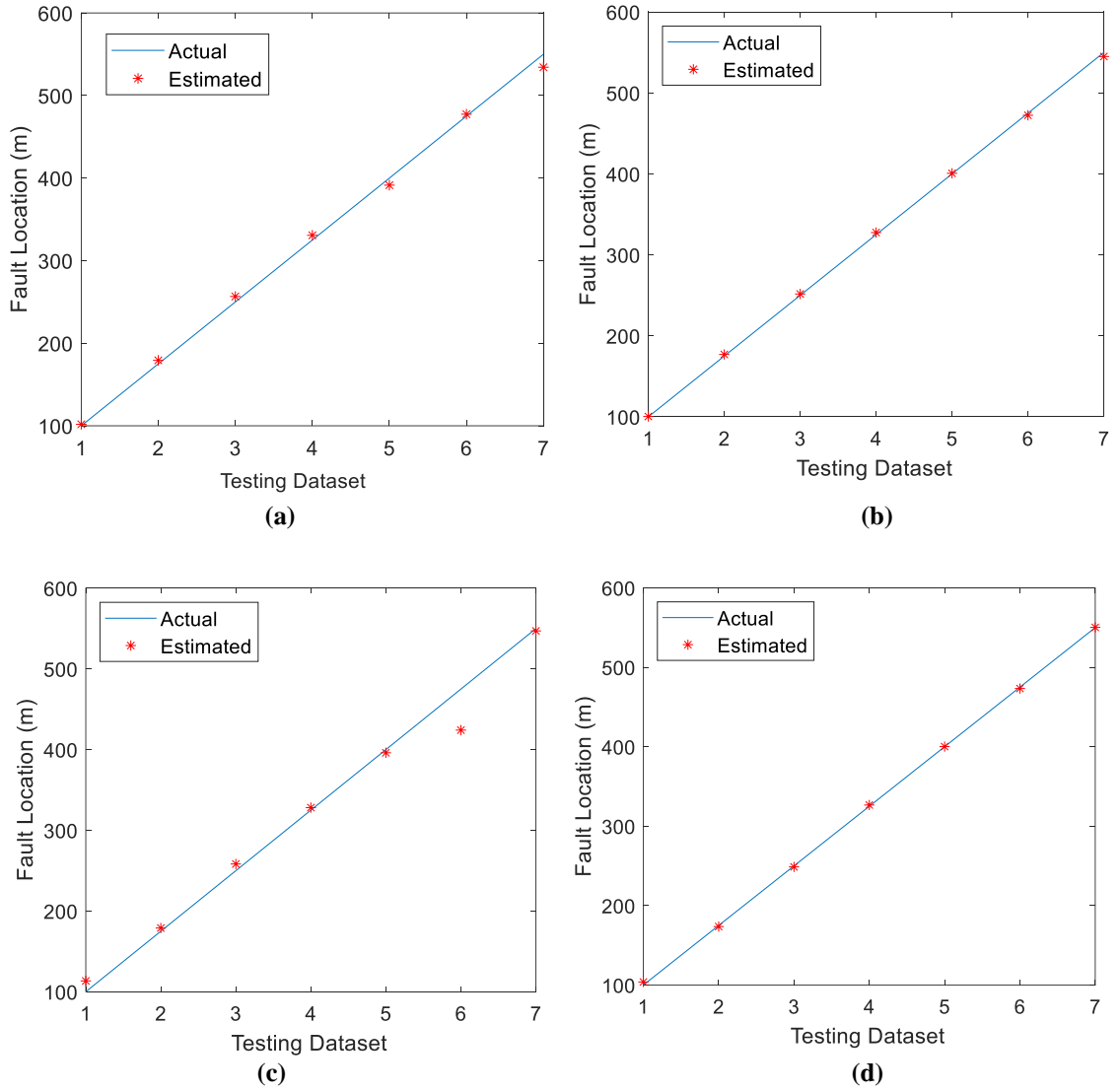
Figure 19. Regression verification plots for C4: (a) bolted PP faults; (b) resistive PP faults; (c) bolted PG faults; (d) resistive PG faults.

Table 3. Fault location estimation error for DC Microgrid 1.

Cable	Bolted PP	Resistive PP	Bolted PG	Resistive PG
C1	4.9%	3.6%	2.5%	4.1%
C2	5.1%	2.9%	3.9%	1.1%
C3	4.7%	6.1%	4%	2.7%
C4	1.1%	0.4%	2.1%	0.2%
C5	6.3%	0.6%	0.8%	0.6%
C6	5.3%	4.8%	6.2%	3.4%

In Table 4, the performance of GP for fault location is compared against some other regression techniques, including Artificial Neural Network (ANN) [62], Decision Tree [63], ε-SVM [64], and Nu-SVM [65]. ANN has been utilized in [38] and [39] for the fault location of DC systems. All ML algorithms were executed in Matlab. To reduce bias, all training and testing data were the same for all methods. The ANN method was executed with the net selected as "fitnet" configured with 10 hidden layers using the "train" function as the training function. The decision tree method was executed with the "fitrtree" function to create the training model and the "predict" function to predict the fault location using the model created from "fitrtree". The ε-SVM and nu-SVM methods are executed with the "svmtrain" function. There are self-selected hyper parameters, c, epsilon, and nu, that must be entered in this function. An iterative loop was constructed to optimize these parameters, which will ensure the lowest amount of error possible. The comparisons are performed for Cable C2. As seen, GP renders higher accuracy compared to the other regression techniques.

Table 4. Comparison of estimation error for different regression techniques for Cable C2.

Fault Type	GP	ANN	Decision Tree	ε-SVM	Nu-SVM
Bolted PP	5.1%	8.6%	9%	8.2%	15%
Resistive PP	2.9%	4.8%	6%	5.9%	14%
Bolted PG	3.9%	8.9%	5.9%	7.7%	9%
Resistive PG	1.1%	2.9%	2.2%	2%	6%

6.2. DC Microgrid 2

The goal of this case study is to verify the performance of the proposed fault location scheme in a microgrid with a meshed topology. To this end, the DC Microgrid 2 shown in Fig. 20 is considered. As seen, this microgrid has a meshed network topology. Herein, the DC microgrid test system in [14] is modified by changing the operating voltage

to 750 V. The nanogrids, AC-DC converter, and cable configuration are similar to the ones in DC Microgrid 1. The microgrid's grounding happens at the middle point of the DC link of the microgrid's AC/DC converter. To verify the effectiveness of the proposed scheme, bolted PP and PG faults are applied at every 50 m of the three cables interconnecting nodes 2, 5, and 6. These three cables form a mesh and are highlighted in red in Fig. 20. In these simulations, DWT's sampling frequency is 1 MHz. Six levels of MRA are used for the fault classification and location algorithm. In Table 5, the fault location estimation errors using GP engines for all cables and different types of faults are summarized. The estimation error percentage is equal to the mean absolute error of the testing dataset over the length of the cable. For each cable, around 65% of the gathered datasets are used for training and the rest are used for testing. The training and testing datasets are selected randomly. The fault location estimation errors in Table 5 verify the effectiveness of the proposed fault location algorithm. The regression results for Relays R25 and R52 are illustrated in Fig. 21. As seen, for both relays, the GP regression engine can effectively locate faults with small estimation errors. In all cases, the proposed algorithm is able to find the fault location in less than 1 ms.

Since a similar microgrid system to [14] is utilized, in Table 5, the fault location accuracy of our proposed scheme is compared against the fault location technique in [14]. It should be noted that, in [14], fault location estimation is only performed for PG faults. Comparing the fault location estimation errors using the fault location algorithm in this thesis against the algorithm proposed in [14], one can see that the estimation errors are very small using both approaches with better accuracies reported for R52, R62, R56, and R65 using the algorithm proposed in this thesis.

46
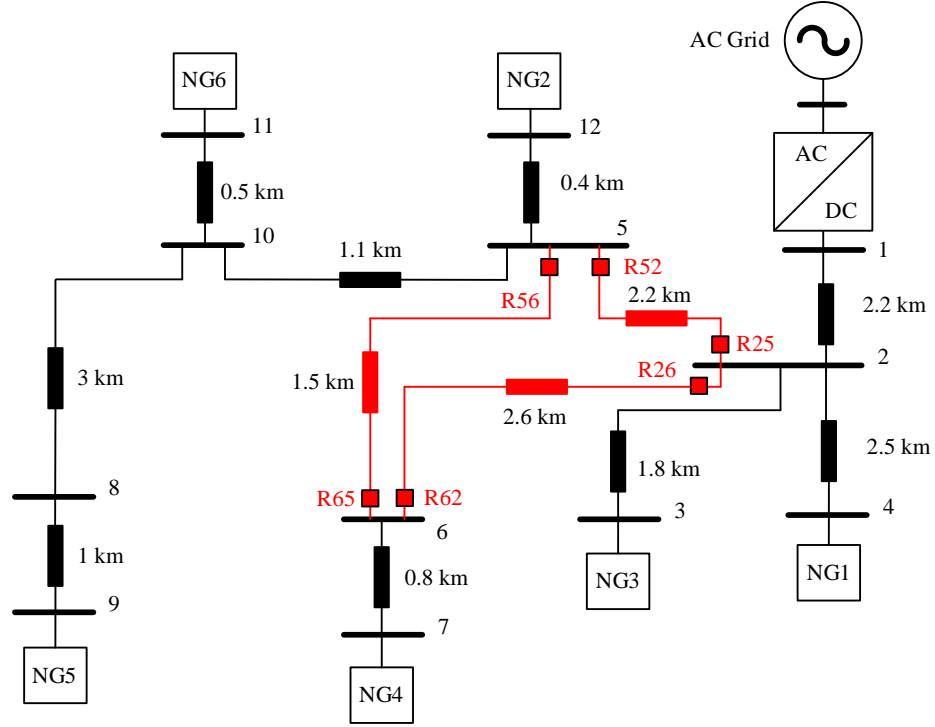
Figure 20. DC Microgrid 2.

Table 5. Fault location estimation error for DC Microgrid 2.

Relay	This Thesis		Reference [14]
	Bolted PP	Bolted PG	Bolted PG
R25	0.26%	0.82%	0.045%
R52	0.27%	0.58%	1.54%
R26	0.42%	0.54%	0.54%
R62	0.39%	0.54%	1.11%
R56	0.46%	0.51%	1.6%
R65	0.69%	0.41%	1.46%
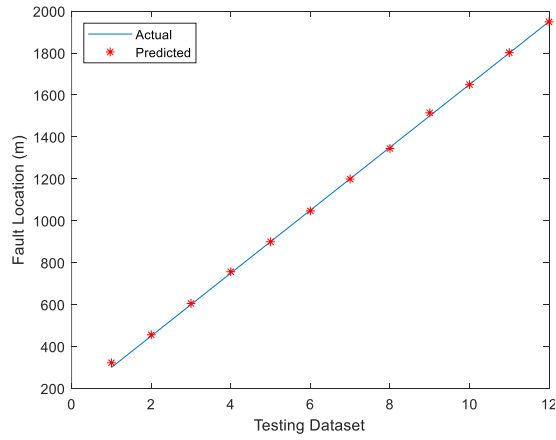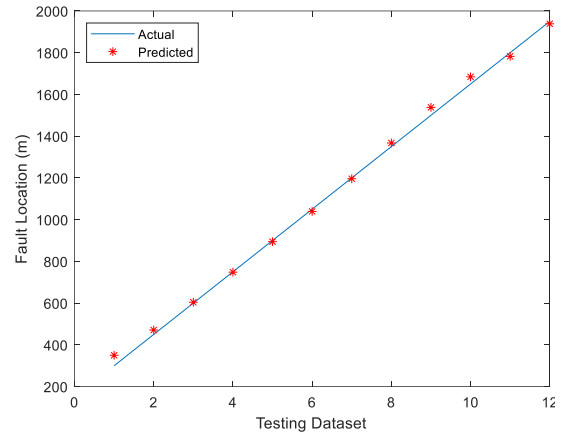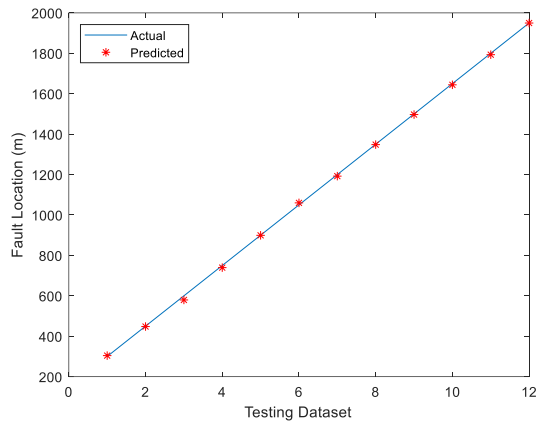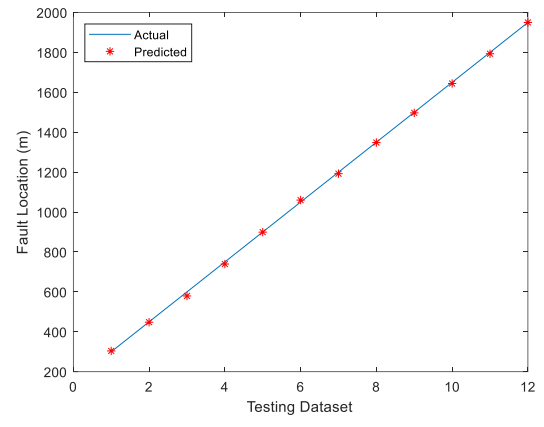
Figure 21. Regression verification plots for Relays R25 and R52: (a) bolted PP faults at Relay R25; (b) bolted PG faults at Relay R25; (c) bolted faults at Relay 52; (d) bolted PG faults at Relay R52.

7. Conclusion and Future Work

In this thesis, a TW-based scheme for fast tripping protection of MV and LV DC microgrids is proposed. The proposed scheme utilizes MRA to calculate the high-frequency components of DC fault currents. The Parseval energy calculated from the MRA coefficients are then calculated, which provide a quantitative relationship between the fault current signal energy and the energy calculated from the MRA's coefficients. The calculated Parseval energy values are used to train an SVM classifier to identify the fault type and a GP regression engine to estimate the fault location on the DC cables. The proposed fault classification and location algorithm: (i) is a single-ended communication-free approach that increases the resilience of the protection systems, and (ii) can effectively work for both bolted and resistive PP and PG faults in LVDC microgrids. The proposed approach was verified by simulating two microgrid test systems in PSCAD/EMTDC. One of the microgrids is radial, and the other one has a meshed topology. The simulation results show that the proposed scheme can effectively identify the fault type and estimate fault locations. The SVM classifier renders 100% precision in distinguishing bolted faults from resistive ones. The GP regression engine is also able to locate faults with an acceptable estimation error range (less than 5% in most of the cases). The case study results show that the GP regression engine renders higher accuracy with a larger number of training datasets. The proposed protection scheme can effectively work with different DWT sampling frequencies. The DWT sampling frequency only impacts the speed of the fault location algorithm. With a higher sampling frequency, MRA is able to calculate the first N levels of wavelet coefficients faster. For example, with 8 MHz sampling frequency and six MRA levels, the proposed algorithm will be able to find the fault location in 200 µs.

This thesis evaluated the effectiveness of using MRA of traveling waves to determine fault locations and types of faults for two different DC microgrid systems. The results were positive and warrant further analysis. Future work based on the result of these findings may include:

- Investigating whether the traveling wave reflections can provide more useful information about the fault location. The traveling wave will remain in the cable and will continuously be reflected back and forth, along the cable and between equipment/transitions, until the wave dissipates with time. Before this dissipation occurs, it may be a possibility that these remaining incidents of traveling waves be used as a subset of training/testing data to identify the fault location. It may be possible that these subsets could be used to create a greater accuracy in predicting fault location at very little increase in computational expense since the data is already being gathered.

- Experimenting with different mother wavelets to determine if there is a better wavelet suited to solve the fault location problem. The Daubechies db8 mother wavelet was used for this analysis but there are many others available and custom ones can be created. Again, the goal here would be to increase accuracy in determining the fault location.

References

[1] R. Montoya, B. Poudel, A. Bidram, M. J. Reno, "DC Microgrid Fault Detection Using Multiresolution Analysis of Traveling Waves," International Journal of Electric Power & Energy Systems, 2022.

[2] P. Buchana and T. S. Ustun, The role of microgrids & renewable energy in addressing Sub-Saharan Africa's current and future energy needs, IREC2015 The Sixth International Renewable Energy Congress, 2015, pp. 1-6, doi: 10.1109/IREC.2015.7110977.

[3] Davidson, Chris. Microgrids: the innovation we need for a livable future. [Online]. Available: https://new.siemens.com/us/en/company/press/siemens-stories/usa/microgrids-the-innovation-we-need-for-a-livable-future.html, accessed March 19, 2022.

[4] Years of fossil fuel reserves left. [Online]. Available: https://ourworldindata.org/fossil-fuels, accessed March 19, 2022.

[5] Z Shahriar Shafiee, Erkan Topal, When will fossil fuel reserves be diminished?, Energy Policy, Volume 37, Issue 1, 2009, Pages 181-189, ISSN 0301-4215, https://doi.org/10.1016/j.enpol.2008.08.016.

[6] Dragicevic T, Lu X, Vasquez JC, Guerrero JM. DC microgrids-Part I: A review of control strategies and stabilization techniques. IEEE Trans Power Electronics 2016; 31(7):4876–91. https://doi.org/10.1109/TPEL.2015.2478859.

[7] Dragicevic T, Lu X, Vasquez JC, Guerrero JM. DC microgrids-Part II: A review of power architectures, applications and standardization issues. IEEE Trans Power Electronics 2016;31(5):3528–49. https://doi.org/10.1109/TPEL.2015.2464277.

[8] Wu D, Tang F, Dragicevic T, Guerrero JM, Vasquez J. Coordinated control based on bus-signaling and virtual inertia for islanded dc microgrids. IEEE Trans Smart Grid 2015;6(6):2627–38. https://doi.org/10.1109/TSG.2014.2387357.

[9] Moayedi SA, Davoudi A. Unifying distributed dynamic optimization and control of islanded DC microgrids. IEEE Trans Power Electronics 2017;32(3):2329–46. https://doi.org/10.1109/TPEL.2016.2565517.

[10] Shadmand MB, Balog RS. Multi-objective optimization and design of photovoltaic-wind hybrid system for community smart dc microgrid. IEEE Trans Smart Grid 2014;5(5):2635–43. https://doi.org/10.1109/TSG.2014.2315043.

[11] Augustine S, Quiroz JE, Reno MJ, Brahma S, DC microgrid protection: Review and challenges, Sandia National Lab, No. SAND2018-8853, 2018.

[12] Shamsoddini M, Vahidi B, Razani R, Mohamed Y. A novel protection scheme for low voltage DC microgrid using inductance estimation. Int J Electr Power Energy Syst 2020;120:105992. https://doi.org/10.1016/j.ijepes.2020.105992.

[13] Naik J, Dhar S, Dash PK, Adaptive differential relay coordination for PV DC microgrid using a new kernel based time-frequency transform, Int J Electr Power & Energy Syst, 2019;106:56-67, http://doi.org/10.1016/j.ijepes.2018.09.043.

[14] Saleh K, Hooshyar A, El-Saadany E. Ultra-high-speed traveling-wave-based protection scheme for medium-voltage DC microgrids. IEEE Trans Smart Grid 2019;10(2):1440–51. https://doi.org/10.1109/TSG.2017.2767552.

[15] Chaudhuri N, Chaudhuri B, Majumder R, Yazdani A. Multi-terminal direct-current grids: Modeling, analysis, and control. Hoboken, NJ, USA: Wiley; 2014. ch. 6.

[16] Hooshyar A, Iravani R. Microgrid protection. Proc IEEE 2017;105(7):1332–53. https://doi.org/10.1109/JPROC.2017.2669342.

[17] Baran ME, Mahajan NR. Overcurrent protection on voltagesource-converter-based multiterminal DC distribution systems. IEEE Trans Power Delivery 2007;22(1): 406–12. https://doi.org/10.1109/TPWRD.2006.877086.

[18] Saleh KA, Hooshyar A, El-Saadany EF. Hybrid passive-overcurrent relay for detection of faults in low-voltage DC grids. IEEE Trans Smart Grid 2017;8(3): 1129–38. https://doi.org/10.1109/TSG.2015.2477482.

[19] Fletcher S, Norman PJ, Fong K, Galloway SJ, Burt GM. High-speed differential protection for smart DC distribution systems. IEEE Trans Smart Grid 2014;5(5): 2610–7. https://doi.org/10.1109/TSG.2014.2306064.

[20] Monadi M, Gavriluta C, Luna A, Candela JI, Rodriguez P. Centralized protection strategy for medium voltage DC microgrids. IEEE Trans Power Delivery 2017;32 (1):430–40. https://doi.org/10.1109/TPWRD.2016.2600278.

[21] Emhemed AAS, Fong K, Fletcher S, Burt GM. Validation of fast and selective protection scheme for an LVDC distribution network. IEEE Trans Power Delivery 2017;32(3):1432–40. https://doi.org/10.1109/TPWRD.2016.2593941.

[22] Bai Y, Rajapakse AD. Fault detection and localization in a ring bus DC microgrid using current derivatives. IEEE Can Conf Electr Comput Eng 2020. https://doi.org/10.1109/CCECE47787.2020.9255718.

[23] Schweitzer EO, Guzman A, Mynam MV, Skendzic V, Kasztenny B, Marx A, Locating ´ faults by the traveling waves they launch, in Proc. 67th Annual Conference for

Protective Relay Engineers, College Station, TX, 2014:95-110, http://doi.org/10.1109/CPRE.2014.6798997.

[24] Aftab MA, Hussain SS, Ali I, Ustun TS. Dynamicprotection of power systems with high penetration of renewables: A review of the traveling wave based fault location techniques. Int J Electr Power Energy Syst 2020;114:105410. https://doi.org/10.1016/j.ijepes.2019.105410.

[25] Jia Q, Dong X, Mirsaeidi S. A traveling-wave-based line protection strategy against single-line-to-ground faults in active distribution networks. Int J Electr Power Energy Syst 2019;107:403–11. https://doi.org/10.1016/j.ijepes.2018.11.032.

[26] Hao W, Misaeidi S, Kang X, Dong X, Tzelipis D. A novel traveling-wave-based protection scheme for LCC-HVDC systems using Teager Energy Operator. Int J Electr Power Energy Syst 2018;99:474–80. https://doi.org/10.1016/j.ijepes.2018.01.048.

[27] Mishra DP, Samantaray SR, Joos G. A combined wavelet and data-mining based intelligent protection scheme for microgrid. IEEE Trans Smart Grid 2016;7(5): 2295–304. https://doi.org/10.1109/TSG.2015.2487501.

[28] Yu JJQ, Hou Y, Lam AYS, Li VOK. Intelligent fault detection scheme for microgrids with wavelet-based deep neural networks. IEEE Trans Smart Grid 2019;10(2): 1694–703. https://doi.org/10.1109/TSG.2017.2776310.

[29] Saleh K. Protection of direct-current systems. PhD Dissertation, Unveristy of Waterloo 2017.

[30] Saleh KA, Hooshyar A, El-Saadany EF, Zeineldin H. Protection of high-voltage dc grids using traveling-wave frequency characteristics. IEEE Syst J 2020;14(3): 4284–95. https://doi.org/10.1109/JSYST.2019.2958811.

[31] Ikhide M, Tennakoon S, Griffiths A, Ha H, Subramanian S, Adamczyk A. Transient-based protection technique for future DC grids utilising travelling wave power, in Proc. In: 14th International Conference on Developments in Power System Protection; 2018. https://doi.org/10.1049/cp.2019.0035.

[32] Wang Y, Hao Z, Zhang B, Kong F. A pilot protection scheme for transmission lines in VSC-HVDC grid based on similarity measure of traveling waves. IEEE Access 2019;7:7147–58. https://doi.org/10.1109/ACCESS.2018.2889092.

[33] Wu J, Li H, Wang G, Liang Y. An improved traveling-wave protection scheme for LCC-HVDC transmission lines. IEEE Trans Power Delivery 2017;32(1):106–16. https://doi.org/10.1109/TPWRD.2016.2549565.

[34] Ma Y, Li H, Wang G, Wu J. Fault analysis and traveling-wave-based protection scheme for double-circuit LCC-HVDC transmission lines with shared towers. IEEE Trans Power Delivery 2018;33(3):1479–88. https://doi.org/10.1109/ TPWRD.2018.2799323.

[35] Azizi S, Sanaye-Pasand M, Abedini M, Hasani A. A traveling-wave-based methodology for wide-area fault location in multiterminal DC systems. IEEE Trans Power Delivery 2014;29(6):2552–60. https://doi.org/10.1109/ TPWRD.2014.2323356.

[36] Tong N, Lin X, Li Y, Hu Z, Jin N, Wei F, et al. Local measurement-based ultra-high-speed main protection for long distance VSC-MTDC. IEEE Trans Power Delivery 2019;34(1):353–64. https://doi.org/10.1109/TPWRD.2018.2868768.

[37] Lu S. DC cable short circuit fault protection in VSC-MTDC. Master's Thesis. Norweigna Univeristy of Science and Technology; 2015.

[38] Li W, Monti A, Ponci F. Fault detection and classification in medium voltage dc shipboard power systems with wavelets and artificial neural networks. IEEE Trans Instrument Measur 2014;63(11):2651–65. https://doi.org/10.1109/ TIM.2014.2313035.

[39] Jayamaha DKJS, Lidula NWA, Rajapakse AD. Wavelet based artificial neural networks for detection and classification of DC microgrid faults. IEEE Power & Energy Society General Meeting (PESGM) 2019. https://doi.org/10.1109/ PESGM40551.2019.8974108.

[40] S. Paruthiyil, R. Montoya, A. Bidram, and M. J. Reno, "A Numerical Method for Fault Location in DC Systems Using Traveling Waves," IEEE North American Power Symposium (NAPS), 2021.

[41] M. Jimenez-Aparicio, M. J. Reno, P. Barba, and A. Bidram, "Multi-Resolution Analysis Algorithm for Fast Fault Classification and Location in Distribution Systems", IEEE International Conference on Smart Energy Grid Engineering (SEGE), 2021.

[42] F. Wilches-Bernal. A. Bidram, M. J. Reno, J. Hernandez-Alvidrez, P. Barba, B. Reimer, R. Montoya, C. Carr, and O. Lavrova "A Survey of Traveling Wave Protection Schemes in Electric Power Systems" IEEE Access, 2021.

[43] Yang H, Liu X, Zhang D, Chen T, Li C, Huang W. Machine learning for power system protection and control. Electricity J 2021;34(1):106881. https://doi.org/ 10.1016/j.tej.2020.106881.

[44] Adewole AC, Tzoneva R, Behardien S. Distribution network fault section identification and fault location using wavelet entropy and neural networks. Appl Soft Comput 2016;46:296–306. https://doi.org/10.1016/j.asoc.2016.05.013.

[45] Malathi V, Marimuthu NS, Baskar S, Ramar K. Application of extreme learning machine for series compensated transmission line protection. Eng Appl Artif Intell 2011;24(5):880–7. https://doi.org/10.1016/j.engappai.2011.03.003.

[46] Livani H, Evrenosoglu CY. A fault classification and localization method for three-terminal circuits using machine learning. IEEE Trans Power Delivery 2013;28(4): 2282–90. https://doi.org/10.1109/TPWRD.2013.2272936.

[47] Livani H, Evrenosoglu CY. A machine learning and wavelet-based fault location method for hybrid transmission lines. IEEE Trans Smart Grid 2014;5(1):51–9. https://doi.org/10.1109/TSG.2013.2260421.

[48] Karmacharya IM, Gokaraju R. Fault location in ungrounded photovoltaic system using wavelets and ANN. IEEE Trans Power Delivery 2018;33(2):549–59. https://doi.org/10.1109/TPWRD.2017.2721903.

[49] Nagam SS, Panda RK, Mohapatra A, Anand S. Gaussian process regression based fault location in DC microgrid. In: 2020 IEEE Texas Power and Energy Conference (TPEC); 2020. https://doi.org/10.1109/TPEC48276.2020.9042542.

[50] Saadat H. Power system analysis, Vol. 2. McGraw-hill; 1999.

[51] Liao CC, Yang H. Recognizing noise-influenced power quality events with integrated feature extraction and neuro-fuzzy network. IEEE Trans Power Delivery 2009;24(4):2132–41. https://doi.org/10.1109/TPWRD.2009.2016789.

[52] Liang J, Elangovan S, Devotta JBX. Application of wavelet transform in travelling wave protection. Int J Electr Power Energy Syst 2000;22(8):537–42. https://doi.org/10.1016/S0142-0615(00)00033-8.

[53] Mallat SG. A theory for multiresolution signal decomposition: the wavelet representation, IEEE Trans. Pattern Anal Mach Intell 1989;11(7):674–93. https://doi.org/10.1109/34.192463.

[54] Perera N, Rajapakse AD, Jayasinghe R. On-line discrete wavelet transform in EMTP environment and applications in protection relaying. International Conference on Power Systems Transients (IPST). 2007.

[55] Daviu JA, Riera-Guasp M, Roger-Folch J, Martínez-Gim´enez F, Peris A. Application and optimization of the discrete wavelet transform for the detection of broken rotor bars in induction machines. Appl Comput Harmon Anal 2006;21(2):268–79. https://doi.org/10.1016/j.acha.2005.12.003.

[56] Bishop CM. Pattern recognition and machine learning. springer; 2006.

[57] [Online]. https://www.mathworks.com/help/stats/support-vector-machines-for-binary-classification.html#bsr5oqx.

[58] Rasmussen CE, Williams CKI. Gaussian processes for machine learning. Cambridge, Massachusetts: MIT Press; 2006.

[59] Altanova Group, "Global monitoring for overhead lines," [Online]. Available: https://www.altanova-group.com/en/products/global-monitoring/tfs-2100-e/, accessed March 25, 2021.

[60] Ning J, Wide-area monitoring and recognition for power system disturbances using data mining and knowledge discovery theory, Ph.D. dissertation, Dept. Comput. Sci., Tennessee Technol. Univ., Cookeville, TN, USA, 2010.

[61] [Online]. Available: https://www.pscad.com/knowledge-base/article/57.

[62] [Online]. Available: https://www.mathworks.com/discovery/neural-network. html.

[63] [Online]. Available: https://www.mathworks.com/help/stats/regressiontree-class. html.

[64] [Online]. Available: https://www.mathworks.com/help/stats/understanding-support-vector-machine-regression.html.

[65] [Online]. Available: https://www.mathworks.com/help/stats/classificationsvm. html.